Anomalous peroxidase activity of cytochrome c is the primary pathogenic target in Barth syndrome

Kagan, Valerian E; Tyurina, Yulia Y; Mikulska-Ruminska, Karolina; Damschroder, Deena; Vieira Neto, Eduardo; Lasorsa, Alessia; Kapralov, Alexander A; Tyurin, Vladimir A; Amoscato, Andrew A; Samovich, Svetlana N

Published in:
Nature Metabolism

DOI:
10.1038/s42255-023-00926-4

Publication date:
2023

nature metabolism

Article

https://doi.org/10.1038/s42255-023-00926-4

Anomalous peroxidase activity of cytochrome c is the primary pathogenic target in Barth syndrome

Received: 8 August 2022

Accepted: 10 October 2023

Published online: 23 November 2023

Check for updates

Valerian E. Kagan[1] ✉, Yulia Y. Tyurina[1], Karolina Mikulska-Ruminska[2], Deena Damschroder[3], Eduardo Vieira Neto[4], Alessia Lasorsa[5], Alexander A. Kapralov[1], Vladimir A. Tyurin[1], Andrew A. Amoscato[1], Svetlana N. Samovich[1], Austin B. Souryavong[1], Haider H. Dar[1], Abu Ramim[6], Zhuqing Liang[6], Pablo Lazcano[6], Jiajia Ji[6], Michael W. Schmidtke[6], Kirill Kiselyov[7], Aybike Korkmaz[8], Georgy K. Vladimirov[1], Margarita A. Artyukhova[1], Pushpa Rampratap[5], Laura K. Cole[9], Ammanamanchi Niyatie[10], Emma-Kate Baker[11], Jim Peterson[1], Grant M. Hatch[9], Jeffrey Atkinson[11], Jerry Vockley[4], Bernhard Kühn[10], Robert Wessells[3], Patrick C. A. van der Wel[5], Ivet Bahar[12], Hülya Bayir[8] ✉ & Miriam L. Greenberg[6] ✉

Barth syndrome (BTHS) is a life-threatening genetic disorder with unknown pathogenicity caused by mutations in *TAFAZZIN* (*TAZ*) that affect remodeling of mitochondrial cardiolipin (CL). TAZ deficiency leads to accumulation of mono-lyso-CL (MLCL), which forms a peroxidase complex with cytochrome c (cyt c) capable of oxidizing polyunsaturated fatty acid-containing lipids. We hypothesized that accumulation of MLCL facilitates formation of anomalous MLCL–cyt c peroxidase complexes and peroxidation of polyunsaturated fatty acid phospholipids as the primary BTHS pathogenic mechanism. Using genetic, biochemical/biophysical, redox lipidomic and computational approaches, we reveal mechanisms of peroxidase-competent MLCL–cyt c complexation and increased phospholipid peroxidation in different TAZ-deficient cells and animal models and in pre-transplant biopsies from hearts of patients with BTHS. A specific mitochondria-targeted anti-peroxidase agent inhibited MLCL–cyt c peroxidase activity, prevented phospholipid peroxidation, improved mitochondrial respiration of TAZ-deficient C2C12 myoblasts and restored exercise endurance in a BTHS *Drosophila* model. Targeting MLCL–cyt c peroxidase offers therapeutic approaches to BTHS treatment.

Barth syndrome (BTHS; MIM: 302060) is an X-linked genetic multisystem disorder caused by mutations in the *TAFAZZIN* (*TAZ*) gene that result in aberrant lipid metabolism. Patients with BTHS exhibit varying degrees of cardiomyopathy, neutropenia, muscle weakness, growth delay, fatigue and exercise intolerance, thus limiting quality of life. Despite improvements in diagnosis, premature death is commonplace due to lack of effective therapies. Clinical trials for two potential BTHS drug treatments, bezafibrate and elamipretide, failed

A full list of affiliations appears at the end of the paper. ✉e-mail: kagan@pitt.edu; hb2753@cumc.columbia.edu; mgreenberg@wayne.edu

to show beneficial effects in their respective trials, with only limited improvement reported for elamipretide in a subsequent trial[1,2]. These results underscore the central problem that the leading pathogenic mechanism of BTHS is unknown. *TAZ* mutations impair remodeling of the mitochondria-specific phospholipid, cardiolipin (CL), which is essential for the normal function of >100 mitochondrial proteins. Consequently, treating secondary effects of TAZ deficiency does not address the underlying pathophysiology. Thus, elucidation of the primary pathogenic mechanism is required to identify therapeutic targets for intervention.

CL is localized almost exclusively in the matrix-facing leaflet of the inner mitochondrial membrane (IMM), accounting for 20–25 mol% of its phospholipids[3]. Combinations of fatty acids in CL's four acyl chain positions result in a myriad of distinct molecular species, with many tissues containing highly diverse CL profiles[4]. Notably, a remarkably uniform CL profile is characteristic of some organs, particularly heart and skeletal muscles of larger vertebrates (including humans), where >80% of all CLs are represented by a single species, tetra-linoleoyl-CL ($CL(L)_4$)[5,6]. While the significance of this uniformity remains enigmatic, it is achieved via an unusual two-stage biosynthetic process: initial biosynthesis of randomly diversified CLs, followed by remodeling, yielding longer-chain polyunsaturated species with a high predominance of $CL(L)_4$ (ref. 7,8).

Remodeling begins with phospholipase A (PLA)-catalyzed CL hydrolysis, producing mono-lyso-CLs (MLCLs) and free fatty acids[7]. This is followed by re-acylation and reconstitution of the tetra-acylated form, ultimately enriching $CL(L)_4$ in heart and skeletal muscles[5]. The identity of the relevant PLA is still conjectural with the notable exception of Cld1 as the confirmed CL-specific PLA in yeast[9]. Re-acylation is catalyzed by one of three enzymes; two of them, mono-lyso-cardiolipin acyl transferase-1 (MLCLAT-1) and lyso-cardiolipin acyl transferase-1 (ALCAT-1), utilize acyl-CoA as substrate, whereas the third, TAZ, utilizes phospholipids for the transacylation reaction[7,10].

While many mitochondrial deficiencies are linked to *TAZ* mutations, distinguishing between the primary pathogenic mechanism of BTHS and secondary consequences of CL–MLCL imbalance has proven difficult. Secondary consequences include dysregulated redox cycling leading to excessive production of reactive oxygen species (ROS) and oxidative injury[11]; however, antioxidant therapies have failed to yield consistently beneficial effects[6]. Our previous work, in model biochemical experiments, has established that CL and MLCL can form a complex with the intermembrane space (IMS) hemoprotein, cytochrome c (cyt c), and that this complex acts as a peroxidase toward polyunsaturated (PUFA)-CL[12,13]. Normally, low levels of MLCL and compartmentalization of CL and cyt c preclude formation of this peroxidase complex; however, TAZ deficiency causes accumulation of MLCL in the IMS-facing leaflet of the IMM, the site of the TAZ-catalyzed reaction[14], making it available to interact with IMS-localized cyt c.

We hypothesized that the formation of MLCL–cyt c complexes serves as the primary pathogenic mechanism in BTHS, realized via oxidation of PUFA phospholipids. We further predicted that mitochondria-targeted ligands capable of suppressing the peroxidase activity of MLCL–cyt c complexes may be effective therapeutics for treating BTHS. Here, we employed genetic, biochemical, biophysical, structural, redox lipidomic and computational modeling approaches to characterize the causative mechanisms and pathogenic role of MLCL–cyt c complexes in BTHS. We discovered that a MLCL–cyt c-mediated pro-oxidant mechanism is responsible for BTHS pathogenesis and that targeting MLCL–cyt c peroxidase offers a potential therapeutic approach to BTHS treatment.

Results

High-spin heme–Fe in MLCL–cyt c peroxidase complex

Binding of anionic molecules to cyt c, including anionic CL, induces rupture of the weak M_{80}–S–Fe axial bond in the protein[15]. This causes a transition from the native hexa-coordinated heme–Fe to a penta-coordinated configuration[16], a requirement for cyt c peroxidase competency[17]. This heme–Fe is characteristic of many non-native cyt c states induced by denaturing agents[18]. In the common ferrous (Fe^{2+}) and ferric (Fe^{3+}) oxidation states, the metal ion typically adopts different configurations of the electron distributions in its d orbitals depending on the strength and number of ligand species bound. In turn, this leads to diagnostically different spectral features, for instance, in the case of the hexa-coordinate 'low-spin' (with one unpaird d electron) ferric heme and the penta-coordinate 'high-spin' (with five unpaired d electrons) peroxidatic ferric heme. We used absorption spectroscopy to distinguish between the high-spin and low-spin ferric hemes in MLCL–cyt c complexes. Addition of tri-linoleoyl-MLCL ($MLCL(L)_3$) to cyt c resulted in the appearance of features typical of the high-spin-state: (1) a weak absorption at 610–620 nm, (2) a more-pronounced shoulder at 560 nm, and (3) a markedly increased absorbance at 495 nm (Fig. 1a). Simultaneously, we observed a decreased absorbance at 695 nm, indicating disruption of the M_{80}–S–Fe bond (Fig. 1b). It is to be understood that these observed changes indicate incomplete reactions; full conversion of low-spin to high-spin ferric heme, for example, would be expected to lead to the complete loss of the 695 nm band rather than the observed partial reduction in intensity (Fig. 1b).

Next, we used electron paramagnetic resonance (EPR) to examine whether the MLCL-induced heme–Fe transition results in 'reprogramming' of cyt c into a peroxidase. Incubation of either

Fig. 1 | Electronic and structural rearrangements occurring in MLCL–cyt c peroxidase complexes. a, MLCL-dependent formation of heme–Fe high-spin forms assessed by absorbance at 620 nm (left). Data are presented as mean ± s.d. ****$P < 0.0001$; one-way analysis of variance (ANOVA) and Tukey's multiple comparison test. $n = 11$ (cyt c), $n = 7$ ($MLCL(L)_3$–cyt c = 1/20) and $n = 8$ ($MLCL(L)_3$–cyt c = 1/30). Each data point represents a biologically independent sample. Effect of MLCL on the absorption spectra of cyt c (75 μM) (middle). The differential absorption spectrum produced by subtracting the spectrum of cyt c from the spectrum of MLCL–cyt c (right). **b**, MLCL induces decrease of the absorption at 695 nm indicating disruption of the M_{80}–S–Fe coordination (left). Data are presented as mean ± s.d. ***$P = 0.0001$, ****$P < 0.0001$; one-way ANOVA and Tukey's multiple comparison test. $n = 12$ (cyt c), $n = 7$ ($MLCL(L)_3$–cyt c = 1/20) and $n = 8$ ($MLCL(L)_3$–cyt c = 1/30). Each data point represents a biologically independent sample. Absorption spectra of cyt c (75 μM) with and without MLCL (right). **c**, Typical EPR signal of *N*-benzyl-*N*-(*tert*-butyl)nitroxide radical generated by $MLCL(O)_4$–cyt c complexes (left, bottom). The underscored part of the spectrum was scanned repeatedly to measure the kinetics of radical formation. Structure of *N*-benzyl-*N*-(*tert*-butyl)nitroxide and its radical are inserted (top). Time courses of *N*-benzyl-*N*-(*tert*-butyl)nitroxide radical EPR signals generated by $MLCL(L)_3$–cyt c and $MLCL(O)_3$–cyt c complexes (right). Control, *N*-benzyl-*N*-(*tert*-butyl)nitroxide radical EPR signals generated by cyt c–H_2O_2 in the absence of MLCL. Data are presented as mean ± s.d. $n = 3$ (control), $n = 4$ ($MLCL(L)_3$) and $n = 4$ ($MLCL(O)_3$) biologically independent samples. a.u., arbitrary units. **d**, Oxidation of BODIPY-C11 by MLCL–cyt c complexes. Data are presented as mean ± s.d. ****$P < 0.0001$; one-way ANOVA and Tukey's multiple comparison test. $n = 4$ (control), $n = 3$ ($MLCL(L)_3$), $n = 6$ ($MLCL(L)_3$–H_2O_2), $n = 9$ (cyt c), $n = 9$ (cyt c–H_2O_2) and $n = 8$ ($MLCL(L)_3$–cyt c), $n = 8$ ($MLCL(L)_3$–cyt c/H_2O_2), $n = 6$ ($MLCL(O)_3$–cyt c), $n = 9$ ($MLCL(O)_3$–cyt c/H_2O_2) biologically independent experiments. Fluorescence emission spectra of BODIPY oxidized by $MLCL(L)_3$–cyt c in the absence and presence of H_2O_2 (excitation of 495 nm) (inset). FAU, fluorescence arbitrary units. **e**, A 2D CP-based ssNMR spectrum of labeled cyt c bound to DOPC:$MLCL(L)_3$ (1:1) vesicles (left). The region marked with a dashed box shows key threonine peaks and is also shown enlarged to the right, with residue assignments indicated. **f**, Structure of cyt c, with color-coding showing relative stability of the native fold segments (colored red < green < blue). The heme group, threonine residues (T_{28}, T_{49}, T_{63} and T_{78}) and Ω-loop residues I_{75} and I_{85} that line the heme-binding pocket are shown as sticks. **g**, A 2D INEPT-TOBSY ssNMR spectrum showing the assignments for observed residues with high flexibility. The ssNMR was performed at 600 MHz (^{1}H) and 253 K (**e**) or 278 K (**g**).

https://doi.org/10.1038/s42255-023-00926-4

$MLCL(L)_3$ or tri-oleoyl MLCL ($MLCL(O)_3$) with cyt c in the presence of *N*-benzyl-*N*-(*tert*-butyl)hydroxylamine generated a one-electron oxidation product with the characteristic nine-line EPR spectrum of *N*-benzyl-*N*-(*tert*-butyl)nitroxide radical (Fig. 1c). The spectrum was interpreted by the coupling of the unpaired electron with the nitrogen nucleus and two equivalent benzylic protons; the spectroscopic parameters are a(N) = 16.76G and a(2Hβ) = 10.62G (1G = 0.1 mT). Both $MLCL(L)_3$–cyt c and $MLCL(O)_3$–cyt c complexes generated *N*-benzyl-*N*-(*tert*-butyl)nitroxide radicals (Fig. 1c) with similar efficiency. We also assessed the peroxidase activity of MLCL–cyt c by monitoring the oxidation of BODIPY-C11 via fluorescence. H_2O_2 caused a significant increase in oxidized BODIPY-C11 fluorescence following

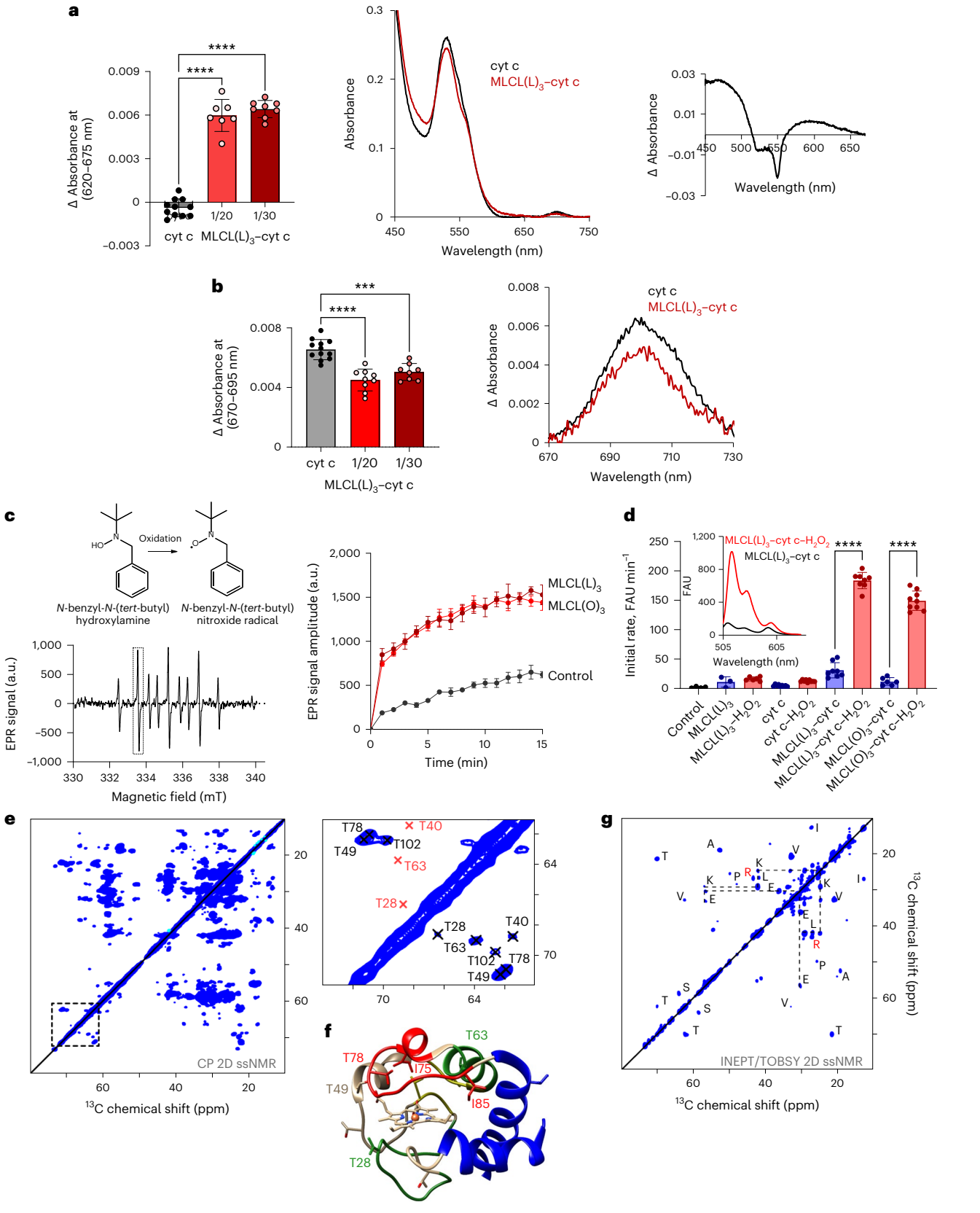

incubation with either MLCL(O)$_3$–cyt c or MLCL(L$_3$)–cyt c complexes. Incubation of BODIPY-C11 with H_2O_2 and MLCL alone had no effect on its fluorescence, suggesting that cyt c is required to confer peroxidase activity to the MLCL–cyt c complex (Fig. 1d).

Solid-state NMR of cyt c binding to MLCL

Next, we probed the impact of MLCL on the molecular structure and dynamics of cyt c protein by solid-state nuclear magnetic resonance (ssNMR) spectroscopy. The ssNMR technique selectively detects the stable-isotope-labeled (^{15}N,^{13}C) protein in its complex with MLCL-containing lipid membranes. In the two-dimensional (2D) ssNMR spectrum (Fig. 1e) we observed numerous off-diagonal peaks from the MLCL-bound protein. Most peak positions match those expected for the cyt c native fold, but this is only true for a subset of the peaks (Extended Data Fig. 1a)[12,19,20]. The intensities of these peaks depend on the rigidity of the observed protein. A subset of strong peaks revealed an immobilized and folded core formed by the N- and C-terminal α-helical segments (Extended Data Fig. 1a,b). These data closely resembled our previous studies of cyt c binding to non-hydrolyzed CL, where we identified a partial unfolding of a specific part of the protein, its so-called Ω-loop D. This loop is the least stable part of the native protein and is functionally relevant (see below). Our current data recapitulate a similar result for the MLCL–cyt c complex; many expected cyt c peaks are diminished or missing, indicating a local loss of stable fold (Fig. 1 and Extended Data Fig. 1c,d). Using threonine (Thr) residues as local probes (Fig. 1e,f) we see evidence for dynamics affecting specific residues (for example Thr$_{28}$ and Thr$_{78}$) as changes in peak height and loss of cross-diagonal symmetry. Thus, different parts of the protein display different extents of motion (detected mobile residues marked red in Fig. 1f). A notable feature of MLCL-bound cyt c is that the Ω-loop becomes much more mobile. This can even be seen in special ssNMR measurements that highlight only the most flexible (not-folded) amino acids, so-called J-based ssNMR (INEPT spectroscopy; Extended Data Fig. 1e)[21,22]. A 2D INEPT-ssNMR spectrum (Fig. 1f) shows only the signals from the labeled protein and reveals surprisingly strong backbone signals, indicating a highly flexible multiresidue segment of approximately 11 residues. This is not seen for CL-bound cyt c (Extended Data Fig. 1f). The chemical shifts and peak patterns for the detected flexible residues identify amino acids that match an extended region from the aforementioned Ω-loop D (between residues I$_{75}$ and I$_{85}$). As expected for flexible segments, these Ω-loop D residues were among the missing or modulated signals mentioned for the 2D spectra (Extended Data Fig. 1c,d) obtained by CP-ssNMR, where we detected the rigid or folded protein parts. We also analyzed the lipid membrane structure and dynamics, using ^{31}P ssNMR that detects only the phosphate head groups of the lipids (Extended Data Fig. 2). The ^{31}P ssNMR lineshapes inform us on the phase and dynamics of the lipids. Inclusion of MLCL gave a new signal with a narrow lineshape indicative of high (head group) motion in a bilayer context[23], which is not seen for normal CL. This bilayer mobilization effect of the lyso-lipid was independent of the effect of cyt c. In summary, ssNMR studies of the MLCL-bound protein show that cyt c retains its most stable folded core, but gains localized flexibility in a particular region (Ω-loop D), with the latter much more pronounced than the motion induced by normal CL[12]. Increased disorder in MLCL-containing membranes (detected by ^{31}P NMR) may underlie these dynamic changes, while also contributing to mitochondrial membrane destabilizing and trans-bilayer CL scrambling.

Molecular dynamics simulations of cyt c binding to MLCL

To examine the interactions between cyt c and MLCL at atomic detail, we performed molecular dynamics (MD) simulations of cyt c interacting with liposomes containing 1,2-di-oleoyl-sn-glycero-3-phosphocholine (DOPC), di-oleoyl-phosphatidylethanolamine (DOPE) and MLCL. MD employs physical and chemical principles to simulate biomolecular systems' dynamics and interactions, providing detailed explanations not attained through experimentation. Among a series of initial MD trajectories, we selected ten in which cyt c diffused toward the membrane bilayer and its positively charged residues and M$_{80}$ interacted with MLCL (Extended Data Fig. 3a). Figure 2 illustrates the summary results from these simulations. We examined cyt c–liposome interactions within two time intervals: (1) initial recognition and membrane binding (during t < 100 ns) (Supplementary Videos 1 and 2), which involved seven positively charged residues, K$_8$, K$_{13}$, K$_{72}$, K$_{73}$ and K$_{86}$–K$_{88}$, along with two hydrophobic residues, I$_{81}$ and A$_{83}$, and two polar residues, N$_{70}$ and Q$_{12}$ (Fig. 2a, top), and (2) stabilization of interactions during the last 100 ns of simulations that exhibited additional hydrophobic contacts with T$_{78}$, M$_{80}$ and F$_{82}$ (Fig. 2a, bottom). The bar plots in the respective panels display the frequency of occurrence of different contacts (different residues along the abscissa and three types of lipid molecules color-coded as labeled) based on snapshots collected at regular (50 ps) intervals during the course of MD simulations. Notably, the initial interactions between cyt c and liposomes were primarily driven by contacts between K$_{86}$–K$_{87}$ and MLCL molecules (Fig. 2a, top), while longer time stabilization also involved various interactions with DOPE and DOPC (Fig. 2a, bottom).

M$_{80}$–MLCL interactions drive the opening of heme-binding pocket

Closer examination of the time evolution of cyt c membrane interactions during MD simulations (Fig. 2b) revealed that the bond Fe–S between the catalytic iron and the S atom of M$_{80}$ exhibited two types of behavior: (1) an increase in the distance between M$_{80}$ and Fe upon the interaction of M$_{80}$ with MLCL (the most frequent behavior); (2) a rupture of the Fe–S bond, inducing a conformational change in the Ω-loop D and insertion of M$_{80}$ into the membrane to interact with multiple MLCL molecules (Supplementary Video 3 and Fig. 2b, bottom).

Fig. 2 | Simulations reveal close association of M$_{80}$ with MLCLs driving the opening of the heme-binding pocket. a, Distribution of contacts between cyt c residues and lipid molecules DOPE, DOPC and MLCL. Membrane-binding residues of cyt c (located within 4.5 Å from the membrane) observed during the first 100 ns (top), and the last 100 ns (bottom) of multiple 700–950-ns long MD simulations were recorded at fixed (50 ps) intervals, to quantitatively determine the most probable interactions. The bar plot shows the number of contacts made by selected cyt c residues (abscissa) with different types of lipid molecules (color-coded as labeled). Red dashed line indicates the threshold for frequent contacts; the corresponding residues are colored red in the ribbon diagram, where the heme group is also displayed in stick representation. **b**, Time evolution of conformational changes in the Ω-loop I$_{75}$–I$_{85}$ (cyan sticks/lines) containing M$_{80}$ (yellow spheres) and its interactions with MLCL, observed during MD simulations (0 < t < 950 ns). The top six panels depict the evolution of interactions, and the bottom plot provides a quantitative summary of the interactions between cyt c residues and multiple MLCL molecules (each shown by a different color). In the top six panels, the lipid bilayer is in surface representation with lipid molecules in sticks at t = 0 (top), and the MLCL is in cyan spheres (with the phosphate groups in red) in all panels except t = 0. The interaction involves various stages: (1) During the first 332 ns the Fe–S bond remains intact. It is completely ruptured at 415 ns, preceded by small extensions at t = 332 and 368 ns; (2) during the interval 415 < t < 500 ns, M$_{80}$ gains an increase in mobility; and (3) at t ≥ 500 ns M$_{80}$ is trapped by several MLCLs (bottom). Time evolution of contacts between cyt c residues and MLCL molecules (different colors for different MLCLs) (bottom). The red arrow points to interactions of M$_{80}$ with multiple MLCLs (atom–atom contacts within 4.5 Å). Supplementary Video 3 shows a visualization. **c**, RMSF profile of cyt c residues in the last 100 ns of two sets of MD runs, one in the presence of membrane (blue curve, averaged over four runs) and the other in water (no membrane) (red curve, averaged over two runs). The crystal structure of cyt c is colored by the relative size of fluctuations (RMSFs in the presence of the membrane minus those in its absence, in Å). Dark red regions (G$_{23}$–H$_{26}$, K$_{72}$ and G$_{77}$–I$_{81}$) exhibit enhanced mobilities in the presence of a membrane upon interactions with MLCL, whereas dark blue regions (K$_8$, K$_{13}$ and K$_{86}$–K$_{88}$) are less flexible being associated with the lipid head groups.

https://doi.org/10.1038/s42255-023-00926-4

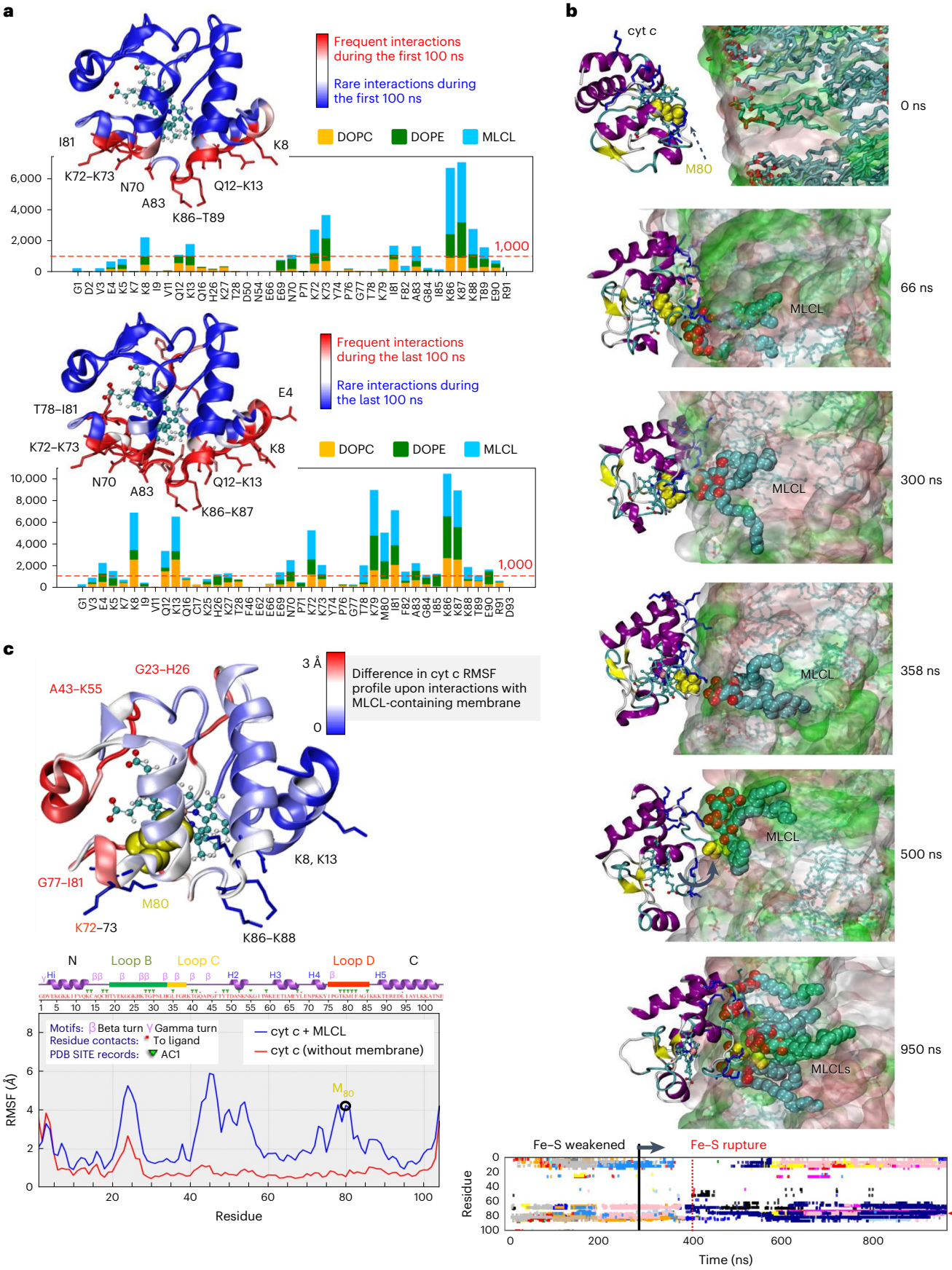

Close association of M_{80} with the membrane was accompanied by partial unfolding of cyt c and exposure of the heme-binding site to the membrane (at $t \geq 500$ ns). Additional simulations carried out in the absence of membrane showed that the positions and interactions between catalytic Fe and S remained unchanged (Extended Data Fig. 3b). This underscores the role of the membrane in regulating the peroxidase activity of the complex.

The presence of MLCL-containing membrane induced robust changes in the mobility of individual parts of cyt c (Fig. 2c). To better understand the scale of these changes, we evaluated the fluctuations of individual residues within protein structure using a measure called root mean square fluctuations (RMSF). RMSF characterizes the flexibility of individual regions within a protein's structure in MD simulations. Assessment of the RMSF of C^{α} atoms in the presence or absence of membrane revealed increased mobility in three cyt c regions primarily induced with the interactions with MLCL: (1) G_{23}–H_{26} (loop B), (2) A_{43}–K_{55} and (3) G_{72}–Y_{74} and G_{77}–I_{81} (Ω-loop D). Overall, these computational results detail the MLCL-induced conversion of cyt c from the hexa- to penta-coordinated state as experimentally observed by ssNMR and electronic spectra.

MLCL–cyt c complexes peroxidize PUFA phospholipids

We next performed liquid chromatography–mass spectrometry (LC–MS) measurements of phospholipid oxidation by MLCL–cyt c complexes. Oxidizable MLCL$(L)_3$ and non-oxidizable MLCL$(O)_3$ were incubated with unilamellar DOPC liposomes in the presence or absence of oxidizable phospholipids, including stearoyl-linoleoyl-phosphatidylethanolamine (SLPE), stearoyl-linoleoyl-phosphatidylcholine (SLPC), stearoyl-arachidonoyl-phosphatidylethanolamine (SAPE) and stearoyl-arachidonoyl-phosphatidylcholine (SAPC). MLCL$(L)_3$–cyt c caused robust MLCL oxidation (Fig. 3a). MS/MS analysis revealed oxygenated MLCL$(L)_3$ with 1–4 oxygens as well as oxidatively truncated species with 9-oxo-nonanoic acid (ONA) formed via degradation of 9-hydroperoxy-(OOH)-linoleic residues (Fig. 3a and Extended Data Fig. 4a). 9-OOH–MLCL$(L)_3$ and di-9-OOH–MLCL$(L)_3$ were the dominant oxidation products. Thus, MLCL$(L)_3$, directly associated with cyt c, is a peroxidation substrate. When peroxidizable PUFA phospholipids that do not bind cyt c (SLPE and SLPC) were incubated with MLCL$(L)_3$–cyt c complexes, MLCL$(L)_3$ oxidation was significantly suppressed (Fig. 3a). 9-OOH–MLCL$(L)_3$ and di-9-OOH–MLCL$(L)_3$ were not detectable in the presence of SLPE. Instead, SLPE and SLPC containing 9-OOH- and 9-hydroxy(OH)-linoleic acid as well as their oxidatively truncated products were detected (Fig. 3b and Extended Data Fig. 4b,c). When non-oxidizable MLCL$(O)_3$ was used instead of MLCL$(L)_3$, PUFA-phospholipid peroxidation was enhanced (Fig. 3b). As both peroxidizable and non-peroxidizable MLCLs are present in cells, we next examined a mixture of 1:3 MLCL$(L)_3$–MLCL$(O)_3$ with cyt c in the presence of SAPE or SAPC. Production of OH and OOH products (predominantly mono-OOH and di-OOH derivatives (Fig. 3b)), as well as oxidatively truncated species (5-hydroxy-8-oxo-6-octenoic acid (HOOA) formed via degradation of OOH-arachidonic acid) was observed. Thus, the peroxidase activity of MLCL–cyt c complexes can catalyze peroxidation of PUFA substrates both within the complex and in the membrane (not directly interacting with cyt c).

TAZ-deficient/Δ^{12}-desaturase yeast cells peroxidize phospholipids

Next, we utilized the genetically tractable yeast model that uniquely enables manipulation of CL remodeling and PUFA-lipid composition and offers two key advantages: (1) the yeast *taz1*Δ mutant exhibits the biochemical manifestations of BTHS, specifically, increased MLCL and decreased CL and (2) although yeast cells only synthesize saturated and Δ^9-monounsaturated fatty acids, we generated wild-type (WT) and *taz1*Δ yeast strains capable of synthesizing PUFAs by expressing the *Hevea brasiliensis* Δ^{12}-desaturase[24]. This system enabled us to determine the specific contribution of PUFA-containing phospholipids to the peroxidation mechanism.

Previously, we showed that the effects of *taz1* deletion were CL-specific, such that levels of other phospholipids, phosphatidylcholine (PC), phosphatidylethanolamine (PE), phosphatidyl-glycerol (PG) and phosphatidylserine (PS), were not altered[24]. As expected, the level of CL was significantly decreased and MLCL content was robustly increased in *taz1*Δ yeast versus WT controls (Fig. 3c and Extended Data Fig. 4d).

To test whether increased MLCL is pivotal in the generation of peroxidase activity independently of PUFA phospholipids, we first employed BODIPY-C11 as an alternative peroxidase substrate and assessed its *tert*-butyl hydroperoxide (tBHP)-induced oxidation in *taz1*Δ versus WT yeast cells. With tBHP as a source of oxidizing equivalents, the peroxidase activity was significantly higher in *taz1*Δ cells, as demonstrated by increased content of oxidized BODIPY-C11 (Fig. 3d). This directly demonstrated that peroxidase activity in *taz1*Δ cells resulted from the mitochondrial accumulation of MLCL despite the absence of PUFA-MLCL and other peroxidizable PUFA phospholipids.

Fig. 3 | Peroxidase activity of the MLCL–cyt c complex causes phospholipid peroxidation in vitro and induces changes in the lipidome and oxylipidome of genetically manipulated yeast. a, MLCL–cyt c complexes cause peroxidation of PUFA phospholipids in a model system. Initial rate of formation of different MLCL$(L)_3$ oxidation products generated by MLCL$(L)_3$–cyt c complexes in the absence and presence of PUFA phospholipids (stearoyl-linoleoyl-PE (SLPE) or stearoyl-linoleoyl-PC (SLPC)). Data are presented as mean ± s.d. Significant differences were determined by unpaired *t*-test. $n = 3$; $^{**}P = 0.0054$ (MLCL$(L)_3$ alone versus MLCL$(L)_3$ + SLPE), $^{**}P = 0.005$ (OH MLCL$(L)_3$ alone versus OH MLCL$(L)_3$ + SLPC), $^{**}P = 0.0039$ (OH/OOH–MLCL$(L)_3$ alone versus OH/OOH–MLCL$(L)_3$ + SLPC), $^{**}P = 0.005$ (OOH–MLCL$(L)_3$ alone versus OOH–MLCL$(L)_3$ + SLPC), $^{****}P < 0.0001$ (2OOH MLCL$(L)_3$ alone versus 2OOH MLCL$(L)_3$ + SLPC). Each data point represents a biologically independent experiment. **b**, Generation of SLPE (top) and SLPC (middle) oxidation products by MLCL$(L)_3$–cyt c and MLCL$(O)_3$–cyt c complexes. Data are presented as mean ± s.d. $n = 3$. Generation of SAPE and SAPC oxidation products by MLCL$(L)_3$–MLCL$(O)_3$ (1:3)–cyt c complexes (bottom). OH (hydroxy), OH/OOH (hydroxy/hydroperoxy), OOH (hydroperoxy), 2OOH (di-hydroperoxy) species, ONA (9-oxo-nanoic acid) and HOOA (5-hydroxy-8-oxooct-6-enoic acid) species. $n = 3$. Each data point represents a biologically independent experiment. **c**, Content of total CL (top) and MLCL (bottom) in WT, *taz1*Δ, Δ^{12}/WT and Δ^{12}/*taz1*Δ yeast cells. Data are presented as mean ± s.d. Significant differences were determined by one-way ANOVA and Tukey's multiple comparison test. $^{**}P = 0.0077$, $^{***}P = 0.0004$, $^{****}P < 0.0001$. Each data point represents a biologically independent experiment. PL, phospholipid. **d**, Detection of lipid peroxidation by BODIPY-C11 581/591 in yeast cells. (Gating strategy is shown in Supplementary Fig. 1.) Oxidation of BODIPY-C11 results in increased fluorescence emission at 510 nm, which is depicted as a rightward shift in the median fluorescence intensity (MFI) histogram (left). The *y* axis corresponds to the number of cells displaying a given MFI (*x* axis). Quantitative assessment of mean fluorescence of shifted peak (right). Data are presented as mean ± s.d. Statistical significance was analyzed using a one- or two-sided Student's *t*-test. $^{**}P = 0.0344$ and $^{***}P = 0.0083$. $n = 3$–4 biologically independent samples. a.u., arbitrary units. **e**, Content of PUFA-CL (top) and PUFA-MLCL (bottom) in WT, *taz1*Δ, Δ^{12}/WT and Δ^{12}/*taz1*Δ yeast cells. Data are presented as mean ± s.d. Significant differences were determined by one-way ANOVA. $n = 3$; $^{****}P < 0.0001$. ND, not detectable. **f**, S-plot of OPLS-DA analysis of Δ^{12}/WT and Δ^{12}/*taz1*Δ yeast lipidomes showing variable correlation versus variable contribution to the OPLS-DA model. **g**, The VIP score plots reflect the significance of variables for the OPLS-DA models. A VIP > 1 was considered to show a statistically significant difference between the two groups. Data are presented for up to 20 phospholipid molecular species. **h**, Volcano plot showing the changes in the levels of oxygenated phospholipid species induced by TAZ deficiency. $n = 3$. Significant differences were determined by unpaired *t*-test. **i**, Content of oxygenated and oxidatively truncated phospholipids in Δ^{12}/WT and Δ^{12}/*taz1*Δ yeast cells. Data are presented as heat maps auto-scaled to z scores and coded blue (low values) to red (high values).

https://doi.org/10.1038/s42255-023-00926-4

To test directly and genetically the importance of cyt c in the formation of the peroxidase complex with MLCL, we monitored the oxidation of BODIPY-C11 in TAZ-deficient yeast lacking functional cyt c. Exposure of *taz1*Δ cells lacking cyt c (*cyc1*Δ) to tBHP resulted in a significant reduction in BODIPY-C11 oxidation versus samples containing functional cyt c (Fig. 3d).

Next, we examined differences in the oxy-lipidome of WT and *taz1*Δ yeast cells expressing Δ^{12}-desaturase (Δ^{12}/WT and Δ^{12}/*taz1*Δ) and hence

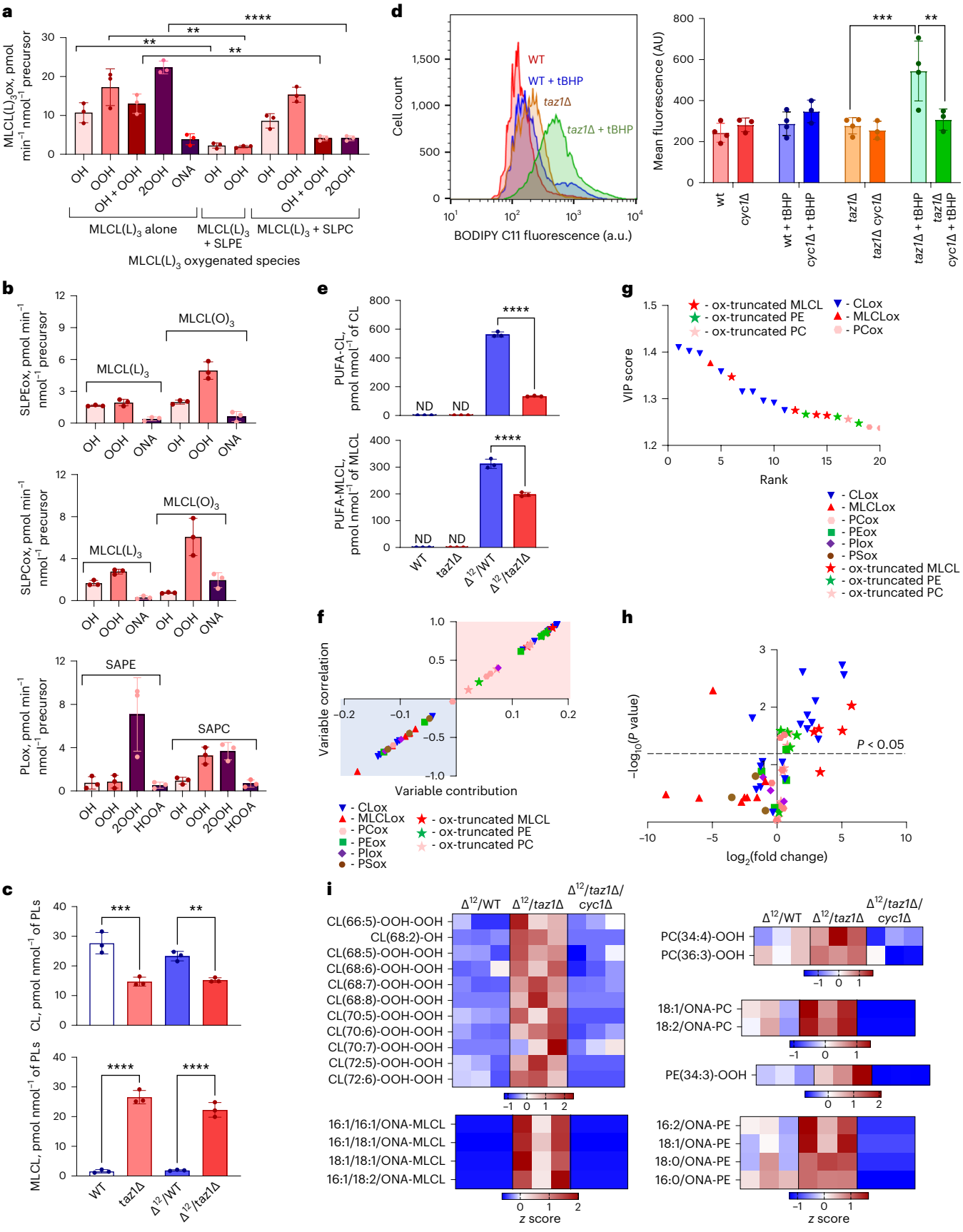

capable of biosynthesizing PUFA phospholipids. Peroxidizable PUFA phospholipids containing C16:2 and C18:2 fatty acids, including CL and MLCL, were present only in Δ^{12}-desaturase-expressing cells (Fig. 3e and Extended Data Fig. 4e,f). Biologically relevant changes were determined using orthogonal projection of latent structures-discriminant analysis (OPLS-DA) (Extended Data Fig. 4g). We found that oxygenated CL and oxidatively truncated phospholipid species, MLCL, PE and PC, were significantly elevated in Δ^{12}/*taz1*Δ cells and had a high variable importance in projection (VIP) score (Fig. 3f–i). The oxy-lipidome of Δ^{12}-desaturase-expressing cells was represented by 60 oxygenated phospholipid species, including 16 oxidatively truncated species (Extended Data Fig. 3h). Of these, 22 species were increased in Δ^{12}/*taz1*Δ cells relative to Δ^{12}/WT cells (Fig. 3h). Oxidized CL was predominant and mainly contained four oxygens, whereas levels of two OOH-PC and one OOH-PE species were also elevated in *taz1*Δ (Fig. 3i). Additionally, the levels of four truncated MLCL, four truncated-PE and two truncated-PC species were significantly elevated (Fig. 3i). All oxidatively truncated phospholipids contained ONA, a product of 9-OOH-linoleic acid degradation. Peroxidation of PS, lacking from mitochondria[25], was not altered in Δ^{12}/*taz1*Δ cells. Cyt c-deficient Δ^{12}/*taz1*Δ cells (Δ^{12}/*taz1*Δ/*cyc1*Δ) neither oxidized PUFA phospholipids nor generated oxidatively truncated phospholipids. This indicates that cyt c–MLCL peroxidase activity is responsible for the accumulation of oxygenated phospholipid species in TAZ-deficient cells (Fig. 3i). Thus, elevated MLCL resulting from TAZ deficiency drives increased mitochondrial phospholipid peroxidation.

PUFA phospholipid peroxidation in TAZ deficiency

The Δ^{12}/*taz1*Δ yeast model produces only two types of oxidizable PUFA phospholipids (containing either C16:2 or C18:2), simplifying the identification of peroxidation products. Because redox lipidomics of TAZ-deficient mammalian tissues with their diverse PUFA phospholipid profile has not been performed before, we examined individual peroxidation products in major phospholipid classes in several types of cells and tissues from mouse and human samples. Mouse samples included myoblasts from WT and TAZ-KO C2C12 cells[26], as well as hearts from WT and TAZ-KD mice[27]. Human samples included lymphoblast lines derived from three affected BTHS individuals and three demographically matched healthy controls, along with heart tissue samples from healthy controls, patients with non-BTHS-associated heart failure (NBHF) and patient with BTHS-associated heart failure (Extended Data Fig. 5a). In all mouse and human samples, TAZ deficiency was associated with decreased CL and elevated MLCL (Fig. 4a). In human heart samples, BTHS tissue exhibited the characteristic decrease in CL and increase in MLCL compared to both control and NBHF samples, which did not differ in their CL profile (Fig. 4a). Thus, decreased CL and increased MLCL are the direct biochemical outcomes of TAZ deficiency.

We next examined levels of bis(monoacylglycero)-phosphates (BMPs), which are excellent biomarkers of autophagy activation as they appear during the fusion of late-endosomes with lysosomes[28], in TAZ-KO versus WT C2C12 cells. We observed accumulation of essentially all BMP molecular species in two major clusters, non-oxidizable (stearic (C18:0), oleic (C18:1)) and highly oxidizable (C20:4) species (Fig. 4b). These data demonstrate a strong activation of autophageal machinery in TAZ-KO versus WT C2C12 cells[29].

A notable increase in the molecular diversification of MLCL and CL was observed in all TAZ-deficient samples, whereby the most characteristic feature was the emergence of polyunsaturated species, especially those containing arachidonoyl-residues (C20:4), which are excellent peroxidation substrates (Fig. 4c, Extended Data Fig. 5b–e and Supplementary Tables 1 and 2). Specifically, TAZ-KO myoblasts exhibited a reduction of C18:2-species and the appearance of MLCL and CL species containing C20:4 (Fig. 4c, Extended Data Fig. 5b and Supplementary Tables 1 and 2). Hearts from TAZ-KD mice also had increased MLCL and CL species containing mostly C20:4, along with linolenic (C18:3) and C18:2 acids (Fig. 4c, Extended Data Fig. 5c and Supplementary Tables 1 and 2). BTHS lymphoblasts contained a higher number of MLCL and CL species predominantly containing C20:4 and C18:3 (Fig. 4b, Extended Data Fig. 5d and Supplementary Tables 1 and 2). Similarly, CL and MLCL species in BTHS hearts were more diverse compared to control and NBHF hearts, including enrichment with C20:4 and C18:3 (Fig. 4c, Extended Data Fig. 5e and Supplementary Tables 1 and 2). An increase in MLCL species with docosapentaenoic (C22:5) and docosahexaenoic (C22:6) acids was observed in hearts from TAZ-KD mice, BTHS lymphoblasts, and BTHS heart samples (Fig. 4c). Collectively, TAZ deficiency resulted in increased levels of readily oxidizable PUFA-containing CL and MLCL species.

We reasoned that MLCL–cyt c peroxidase activity and increased peroxidizable lipid substrates in TAZ-deficient cells should lead to the accumulation of peroxidized PUFA phospholipids (Fig. 4d and Extended Data Fig. 5f). Comparison of the oxi-lipidomes of WT and TAZ-KO mouse myoblasts and WT and TAZ-KD mouse heart samples using OPLS-DA (Extended Data Fig. 5g) showed that the levels of 32 species were significantly elevated in TAZ-KO cells compared to WT and more than half of these were also upregulated in TAZ-KD hearts (Fig. 4d). Human samples showed a similar pattern of oxidized lipid enrichment (Extended Data Fig. 5g). Specifically, 25 oxygenated species were upregulated in BTHS lymphoblasts, and 43 and 23 species were upregulated in BTHS hearts compared to control or NBHF tissue, respectively (Fig. 4c). Control and NBHF tissue samples did not differ significantly with respect to oxidized lipids.

In TAZ-deficient mouse myoblasts and heart tissues (Fig. 4e,f) as well as in BTHS lymphoblasts and heart biopsy samples (Fig. 4g,h), oxygenated phospholipids were mainly represented by MLCL, CL,

Fig. 4 | TAZ deficiency induces changes in the phospholipidome of mouse and human cells and tissues. a, Content of MLCL and CL in C2C12 cells, mouse heart, human lymphoblasts and human heart samples. Two-tailed *t*-test, for MLCL, $^{***}P = 0.0002$, $^{****}P < 0.0001$, one-way ANOVA, Tukey's multiple comparison test. For CL, $^{*}P = 0.0189$ (unpaired two-tailed *t*-test), $^{**}P = 0.0009$, $^{***}P = 0.0002$, $^{****}P < 0.0001$, one-way ANOVA, Tukey's multiple comparison test. Data are presented as mean ± s.d. $n = 3$ biologically independent cells, $n = 3$ and $n = 5$ biologically independent control and TAZ-KO mice, respectively, $n = 3$ biologically independent human lymphoblasts and $n = 3$ biologically independent human heart biopsy samples. **b**, Content of BMP in WT and TAZ-deficient cells. Data are presented as heat maps auto-scaled to *z* scores and coded blue (low values) to red (high values). **c**, Number of PUFA-MLCL (top) and PUFA-CL (bottom) species in C2C12 cells, mouse heart, human lymphoblasts and human heart. **d**, Volcano plots showing significant changes in the levels of oxygenated PL species induced by either TAZ deficiency in cells and mouse heart or TAZ mutation in human lymphoblasts and heart samples from patients with BTHS. $n = 3$–5. Significant differences were determined by an unpaired two-tailed *t*-test. **e**–**h**, Content of oxygenated PLs in WT and TAZ-deficient cells (**e**), heart tissue obtained from WT and TAZ-KD mice (**f**), control and BTHS lymphoblasts (**g**) and control, NBHF and BTHS heart samples (**h**). Data are presented as heat maps auto-scaled to z scores and coded blue (low values) to red (high values) (left), and bar graphs of the VIP score plots that reflect the significance of variables for the OPLS-DA models (right). **i**, The two-way Venn diagram congregated oxygenated molecular species of phospholipids detected in TAZ-KO C2C12 myoblasts in vitro and heart of TAZ-KD mice in vivo. Six species (MLCL(52:6)-2OOH, PE(36:4)-OOH, PC(38:5)-OH, PE-16:0/ONA, PC(38:6)-OH and PC(40:7)-OH) common to TAZ deficiency were identified. The value in each area indicates the number of oxygenated molecular PL species with significantly higher levels in TAZ groups versus WT by unpaired two-tailed *t*-test. **j**, A two-way Venn diagram congregated oxygenated molecular species of PLs detected in BTHS lymphoblasts and BTHS hearts. Seven MLCL species common to BTHS (MLCL(54:6)-2OOH, MLCL(54:7)-2OOH, MLCL(56:7)-OOH, MLCL(56:8)-OOH, MLCL(54:5)-2OOH, MLCL(58:9)-OOH and MLCL(18:1/18:1/ONA)) were identified. The value in each area indicates the number of oxygenated molecular PL species with significantly higher levels in BTHS groups versus respective control by unpaired two-tailed *t*-test.

https://doi.org/10.1038/s42255-023-00926-4

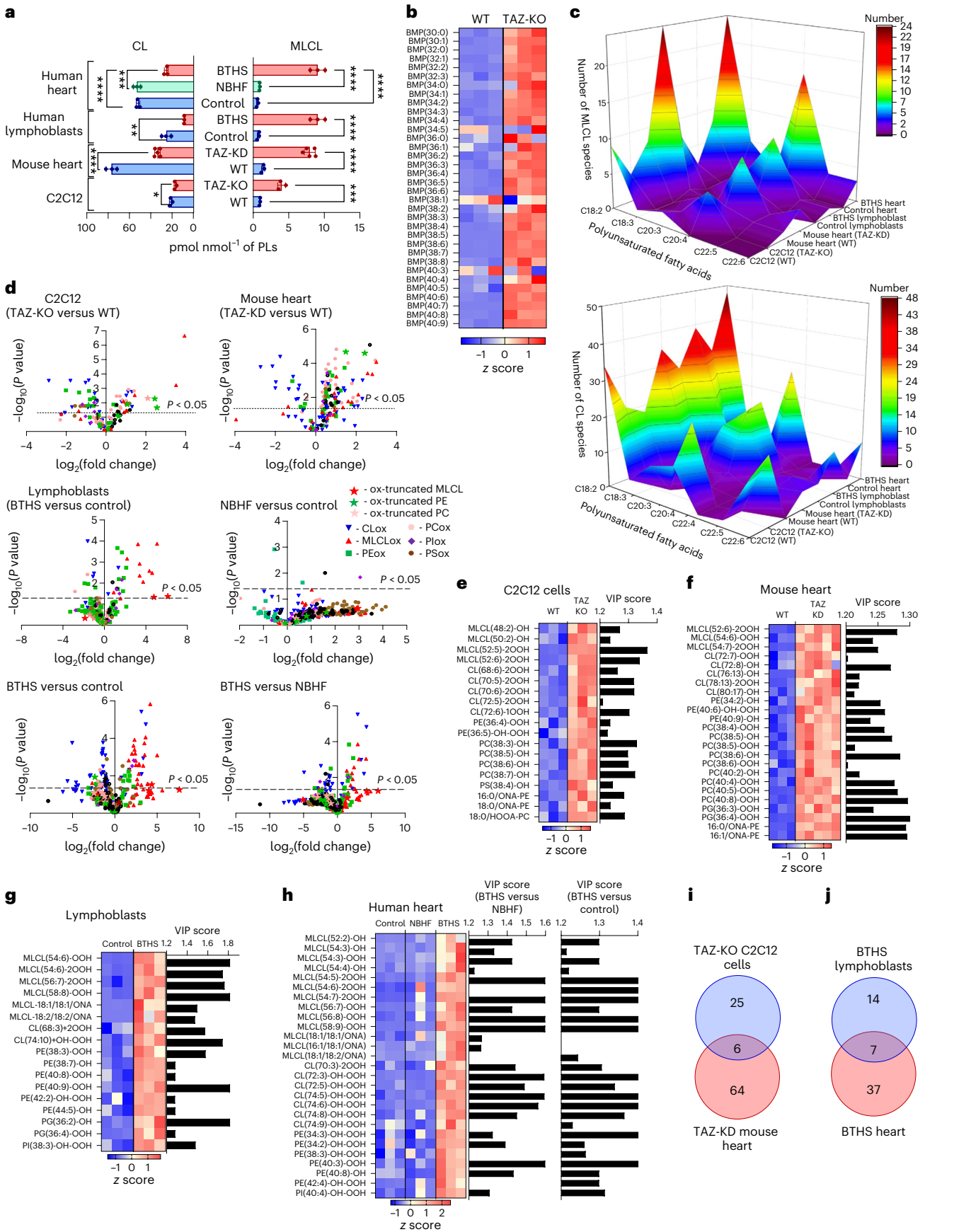

PE and PC. Among these, oxygenated species of MLCL, CL and PE differed the most between BTHS and controls, resulting in a high VIP score (>1.2) (Fig. 4e–h). Oxygenated MLCL and CL originated predominantly from C20:4-containing species. No significant differences in oxygenated PS were detected in any of the TAZ-deficient samples. Because PS is localized primarily outside of mitochondria, this suggests that BTHS-associated lipid oxidation takes place mainly in mitochondria. The predominance of peroxidized MLCL suggests that peroxidation occurs primarily within MLCL–cyt c complexes, whereas the presence of other oxidized phospholipids indicates that peroxidation also occurs outside of the complex. While the quantitative assessment of non-oxidized major phospholipids, PC and PE, revealed small changes in their content, the variety of individual molecular species and their distribution were cell and tissue dependent (Extended Data Fig. 6).

Next, we identified overlapping lipid species that were enriched across sample types using a two-way Venn diagram. Analysis of oxygenated lipids from mouse myoblasts and hearts revealed six shared species of oxygenated lipids elevated in both TAZ-deficient models relative to controls, including MLCL(52:6)-2OOH, PE(36:4)-OOH, PC(38:5)-OH, PE-16:0/ONA, PC(38:6)-OH and PC(40:7)-OH (Fig. 4i). A similar analysis of overlapping species in human samples revealed seven oxygenated species common to both BTHS lymphoblasts and BTHS heart tissue: MLCL(54:6)-2OOH, MLCL(54:7)-2OOH, MLCL(56:7)-OOH, MLCL(56:8)-OOH, MLCL(54:5)-2OOH, MLCL(58:9)-OOH and MLCL(18:1/18:1/ONA) (Fig. 4j). No other oxygenated phospholipids were common to BTHS lymphoblasts and BTHS heart tissue. Thus, MLCL oxidation, likely occurring within MLCL–cyt c complexes, is a hallmark of the BTHS lipidome and may serve as a BTHS biomarker.

IOA suppresses MLCL–cyt c peroxidase activity

If MLCL–cyt c peroxidase activity is the primary driver of BTHS pathogenesis, its inhibitors should prevent the injurious effects of TAZ deficiency. We previously established that a mitochondria-targeted Fe-ligand, imidazole oleic acid (IOA), can reconstitute the hexa-coordinated low-spin Fe in the complex and inhibit its peroxidase activity[30]. Therefore, we tested whether IOA can suppress the MLCL-driven conversion of cyt c into a peroxidase.

IOA prevents MLCL–cyt c phospholipid peroxidation

We first asked whether IOA could convert the MLCL–cyt c complex to some non-peroxidase state in biochemical models. IOA attenuated the MLCL$(L)_3$-induced changes in absorbance at 620 nm by 35% (Fig. 5a), consistent with interaction of the IOA imidazole moiety with the heme–Fe, and decreased the absorbance at 695 nm, suggesting that liganding of heme–Fe by imidazole occurred rather than the native Fe–M_{80} interaction (Fig. 5b). We demonstrated that effective inhibition of CL–cyt c peroxidase activity requires targeted delivery of IOA into mitochondria by conjugating it with triphenyl-phosphonium (TPP)[30]. TPP–IOA acted similarly to IOA alone, indicating that TPP had a negligible effect on the interaction of IOA with both MLCL$(O)_3$–cyt c and MLCL$(L)_3$–cyt c complexes (Extended Data Fig. 7a,b). Consequently, oxidation of *N*-benzyl-*N*-(*tert*-butyl)hydroxylamine by MLCL$(O)_3$–cyt c peroxidase activity was also strongly suppressed by IOA (Fig. 5c). Furthermore, IOA and TPP–IOA effectively inhibited the MLCL$(L)_3$–cyt c-induced accumulation of phospholipid oxidation products in a concentration-dependent manner, including HOO-MLCL$(L)_3$ and HOO-PE as well as their oxidatively truncated species (Fig. 5d and Extended Data Fig. 7c).

ssNMR reveals IOA localization at heme cavity

In the presence of IOA, 2D ssNMR revealed a specific set of residue-specific spectral changes in MLCL-bound cyt c (Fig. 5e; orange) compared to control (black). Most notable were changes in peak position and intensity for residues I_9, I_{75} and I_{85} (dashed ovals). Changes in peak position indicate changes in local structure and/or dynamics, whereas the intensity changes stem from a change in local motion. Elsewhere in the protein, the (Thr) peak intensities (Fig. 5f and Extended Data Fig. 7d) revealed minimal changes, meaning that the IOA did not modulate overall protein motion and illustrating the high reproducibility in the measurements. In contrast, the clear IOA-induced reduction in the intensities of the I_{75} and I_{85} peaks indicates increased local motion near those amino acids located in the Ω-loop D. Thus, we were able to see by NMR, the localized impact of IOA on hydrophobic residues in the protein's Ω-loop D (I_{75}–I_{85}), near the heme cavity (shown in red in Fig. 5g).

MD simulations of MLCL–cyt c complexes plus IOA

We further analyzed the conformational dynamics of the cyt c–IOA complex (Fig. 5h). The initial configuration of the system was obtained by molecular docking simulations of IOA onto an open conformation of cyt c (Fig. 2b; 950 ns). Docking simulations usually identify the binding poses of small molecules onto target proteins provided that those sites are solvent-accessible, but those binding events involving the insertion of the small molecule into relatively buried (cryptic) pockets require previous opening of the target protein pocket to expose the binding site. In this case, the disruption of the Fe–S bond was required for the insertion of IOA into the close proximity of the catalytic Fe; hence we used the partially relaxed/unfolded conformation of cyt c obtained at the end of the 950-ns simulations (Fig. 2b). This permitted us to target the vicinity of the Fe–S bond and visualize the mechanism of binding of IOA to cyt c. Similar to a previous study[30], we observed that L_{68}, K_{13} and Ω-loop D had the most significant effect on the coordination of IOA by cyt c residues; however, current simulations indicated a shorter distance of 2.1 ± 0.2 Å between the imidazole N and the catalytic Fe in two alternative bound conformations of IOA (type 1 and 2 binding, with the negatively charged end of IOA facing in opposite directions; left and right in Fig. 5h and inset). This distance is even shorter than

Fig. 5 | Effect of TPP–IOA on the structure of MLCL–cyt c peroxidase complexes, lipid oxidation. a,**b**, Effect of IOA on MLCL-dependent formation of heme–Fe high-spin forms (**a**) and the absorbance at 695 nm (**b**). Representative absorption spectra of MLCL–cyt c with or without IOA (right panels). Data are presented as mean ± s.d. $n = 11$ (cyt c), $n = 7$ (IOA–cyt c = 2/1), $n = 8$ (IOA–cyt c = 4/1). Each data point represents a biologically independent sample. $^{****}P < 0.0001$. Data were analyzed by one-way ANOVA and Tukey's multiple comparison test. **c**, Time courses of *N*-benzyl-*N*-(*tert*-butyl)nitroxide radical EPR signal formed by MLCL$(O)_3$–cyt c in the absence (dark red) and presence (light red) of IOA (10 μM). Data are presented as mean ± s.d. $n = 3$. Data were analyzed by one-way ANOVA and Tukey's multiple comparison test. $^{****}P < 0.001$. Each data point represents a biologically independent sample. **d**, TPP–IOA inhibits accumulation of hydroproxy-MLCL species MLCL$(L)_3$-OOH (left), di-hydroperoxy MLCL species MLCL$(L)_3$-OOH-OOH (middle) and oxidatively truncated MLCL$(L)_3$-ONA species (right) formed in the MLCL$(L)_3$–cyt c-driven reaction. $n = 3$. Data are presented as mean ± s.d. Data were analyzed by one-way ANOVA and Tukey's multiple comparison test. For MLCL$(L)_3$-OOH $^{***}P = 0.001$, $^{****}P < 0.0001$. For MLCL$(L)_3$-OOH-OOH $^{*}P = 0.032$, $^{****}P < 0.0001$. For MLCL$(L)_3$-ONA $^{*}P = 0.0109$, $^{**}P = 0.0042$. Each data point represents a biologically independent sample. **e**, The 2D CP-ssNMR spectra (left) and zoomed regions (right) for labeled cyt c bound to DOPC:MLCL (2:1) vesicles in the absence (black) and presence (orange) of 4× excess IOA. Dashed oval (far right) marks peaks for Ile_{75}/Ile_{85} that are missing in the IOA sample. **f**, Normalized peak intensity in the absence (black) and presence (orange) of IOA, for Thr Cα/β peaks and Cβ/γ of Ile_{75} and Ile_{85}. Differences indicate changes in local molecular motion. **g**, Image of the unbound fold of cyt c, with inset showing Ile_{75} and Ile_{85} (in sticks) and the Ω-loop (red) in between. **h**, Two different binding poses of IOA, bound to cyt c, obtained by docking simulations followed by MD runs: type 1 (seven runs, left) and type 2 (three runs, right). Type 2 occasionally exhibited a flip to type 1 (the thin sticks showing the alternative conformation). The residues that were distinguished by their high contact frequencies (normalized with respect to the top-ranking residue) are displayed in the bar plots, in decreasing frequency of contacts. The distance between the N atom of the imidazole and Fe^{3+} ion is shown in the black histograms (inset, the last 100 ns of each set of simulations).

https://doi.org/10.1038/s42255-023-00926-4

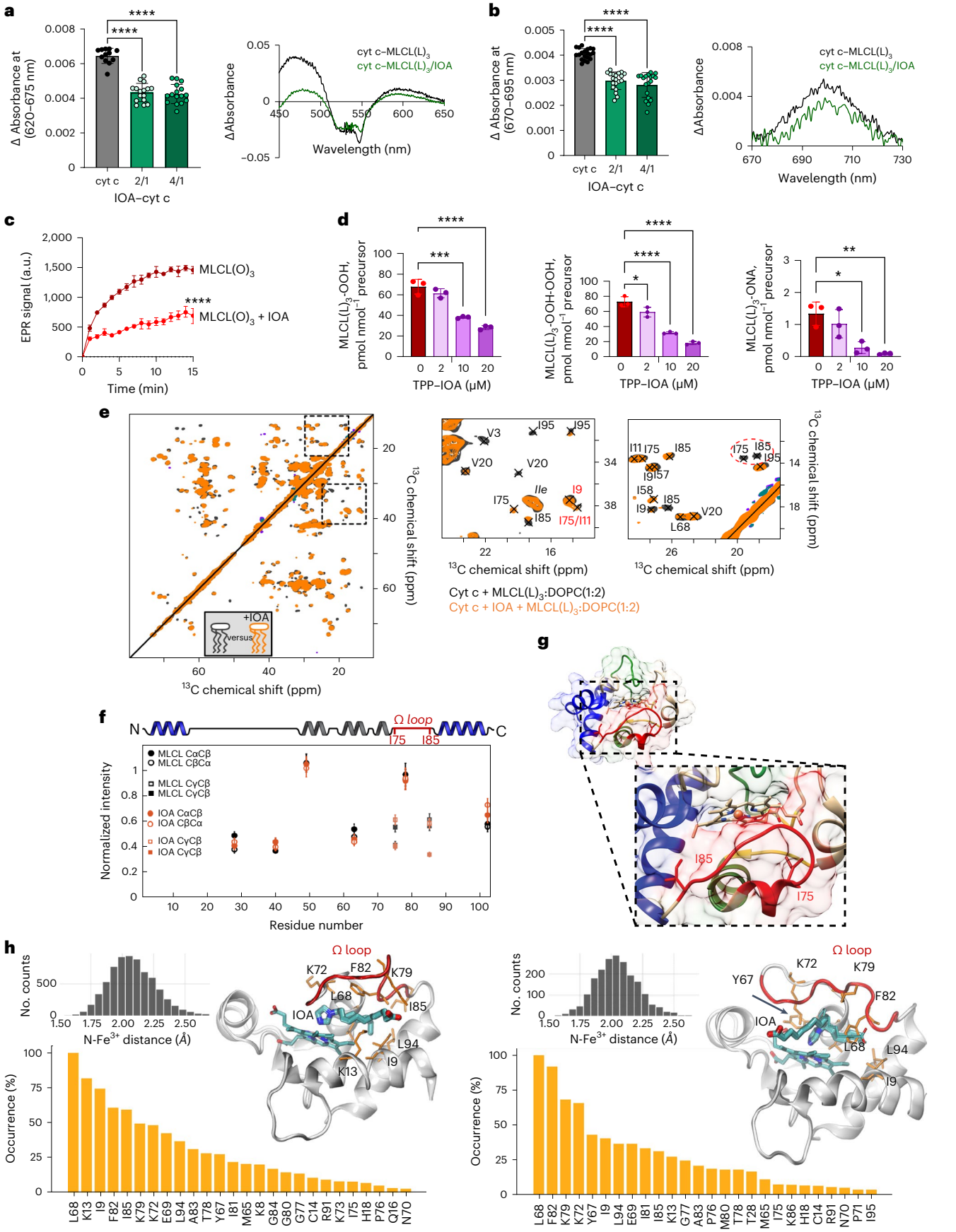

that of the Fe–S bond (~2.5 ± 0.1 Å). This indicates that IOA interacts with cyt c by utilizing the imidazole group as the sixth ligand to the heme–Fe and that the conformational flexibility near the Ω-loop D and the overall relaxation of cyt c achieved in MD simulations is critical to expose additional crucial residues for IOA coordination, such as I_9, K_{72}, K_{79} and Y_{67} (type 1).

Mitochondria-targeted TPP–IOA rescues fatigue in TAZ-deficient flies

The pivotal test of our hypothesis was to determine whether suppression of MLCL–cyt c peroxidase activity ameliorates the pathological outcome of BTHS. Therefore, we examined the potential of TPP–IOA to rescue motor dysfunction in the *Drosophila* model of BTHS. Previous studies reported that *Drosophila* TAZ mutants exhibit motor weakness[31], and this powerful functional model has been utilized previously to test therapeutic modalities for BTHS[32]. TAZ^{889} mutant flies showed reduced endurance relative to w^{1118} control flies (Fig. 6a). Detailed oxy-lipidome comparison between WT and mutant flies indicated that impaired endurance was associated with a decrease in CL and increase in MLCL (Fig. 6b and Extended Data Fig. 8a,b). TAZ deficiency resulted in a greater diversity of oxidizable PUFA-CL–MLCL species. Specifically, an increased number of CL and MLCL species containing C18:2 and C18:3 fatty acids were detected in TAZ-deficient flies (Fig. 6c and Extended Data Fig. 8c,d). Furthermore, mutant flies showed an accumulation of lipid peroxidation products, including oxygenated MLCL, PE, PC (Fig. 6d) and oxidatively truncated MLCL and PE species (Fig. 6e). Notably, TPP–IOA had a strong positive effect on the endurance of flies. TAZ^{889} flies fed TPP–IOA for either 10 or 17 d showed markedly enhanced endurance relative to vehicle-fed controls (Fig. 6f, top and bottom, respectively). TPP–IOA did not affect the endurance of control flies (Extended Data Fig. 8e). TPP–IOA also restored levels of both CL and MLCL in mutant flies (Fig. 6g) and reduced levels of lipid peroxidation products (Fig. 6h). In contrast, TPP–IOA administration had no effect on CL and MLCL content in control flies (Extended Data Fig. 8f). No toxic effects of TPP–IOA were observed in experiments with *Drosophila*, and we noted no apparent loss of endurance in WT flies that received TPP–IOA, suggesting that oxidative phosphorylation was not inhibited by our treatment regimen.

IOA improves respiratory parameters in TAZ-KO cells

In agreement with our hypothesis, we found that TAZ deficiency was associated with impairment of several mitochondrial respiratory parameters, which were positively affected by the treatment of TAZ-KO C2C12 cells with the peroxidase inhibitor, IOA (Fig. 7a–e). Notably, increases in these parameters were also detected in WT C2C12 cells (Fig. 7). No toxicity was observed after treatment of C2C12 cells with IOA in sub-micromolar concentrations (employed as a complex with fatty-acid-free BSA) over the course of 5 d. To further characterize functional impairments of mitochondria in TAZ-deficient C2C12 cells, we performed measurements of the mitochondrial membrane potential of WT and TAZ-KO cells using fluorescence of tetramethylrhodamine methyl ester (TMRM), a cell-permeant dye that accumulates in mitochondria in proportion to their membrane potential[33]. Using flow cytometry, we found a significant decrease in the membrane potential of TAZ-KO C2C12 cells, detected as a shift in the number of cells with lowered mean fluorescence intensity compared to WT cells (Fig. 7f). Treatment with IOA decreased this shift in both WT and TAZ-KO cells, reflecting an increase in the number of cells with a higher membrane potential (Fig. 7f,g).

Discussion

Many mitochondrial impairments have been implicated in the overall pathogenic mechanism of BTHS; however, these studies failed to identify a direct (primary) mechanistic link between the impairments and the root cause of BTHS, deficient tafazzin transacylase activity, and instead only invoke disrupted mitochondrial structure/function as the precipitating cause. The main barrier to the development of effective therapies has been the gap in understanding the primary pathogenic mechanism underlying the disorder. Consequently, current therapies only reduce symptoms without curing the disease. The loss of CL and accumulation of MLCL, the major pathognomonic metabolic abnormality in BTHS, leading to ROS production and oxidative stress, have been associated with the disease[34]; however, the mechanism linking these conditions to the pathology has not been identified and genotype–phenotype correlations have not been demonstrated. A recent elamipretide clinical trial[1] showed no significant beneficial effect of the drug following the randomized, double-blind, placebo-controlled part 1, although a limited beneficial effect was reported following the part 2 open-label extension, in which all participants received the drug with no placebo control group[35].

Our work discovered that the massive enrichment of MLCL makes it available to form complexes with the IMS hemoprotein, cyt c, thus converting the latter into an anomalous peroxidase capable of catalyzing peroxidation of mitochondrial PUFA phospholipids. We identified the mechanisms that initiate MLCL–cyt c complex peroxidase competency. Normally, cyt c maintains the hexagonal organization of its heme–Fe, which does not support peroxidase activity, but is optimized to act as a shuttle of electrons between mitochondrial complexes III and IV[36]. Disordering or denaturing of the protein (for example, by nitration, phosphorylation and sulfoxidation of specific amino acids, high temperature, acids, bases and anionic lipids) results in the transition of the protein into a penta-coordinate high-spin form whereby the heme–Fe is capable of interactions with H_2O_2 and organic (including lipid) hydroperoxides[37–42]. This is accompanied by a gain of peroxidase function[43,44]. Notably, negatively charged hydroperoxy-phospholipids, particularly CL and MLCL, are effective in causing these structural rearrangements of cyt c[17,45]. Furthermore, hydroperoxy-CL can also be utilized as a source of oxidizing equivalents, feeding the peroxidase reaction of the cyt c–CL complexes[46]. As a result, peroxidized CL (and MLCL) formed by the peroxidase activity of the complex may

Fig. 6 | TAZ deficiency induces changes in *Drosophila* endurance and the *Drosophila* lipidome. a, TAZ^{889} mutants have reduced endurance relative to control w^{1118} flies. Time to fatigue was quantified as the time when less than 20% of flies in a vial were still running. Each vial of 20 flies was treated statistically as a single independent replicate ($n = 8$ biological replicates for each group). Significance was determined by log-rank analysis. $^{**}P = 0.0027$. **b**, Content of CL (top) and MLCL (bottom) in control w^{1118} and TAZ^{889}-deficient flies. Data are presented as mean ± s.d. CL, $^{**}P = 0.0020$; MLCL/CL, $^{**}P = 0.0022$, unpaired two-tailed *t*-test. **c**, Quantitative characterization of CL and MLCL molecular species containing poorly oxidizable monounsaturated fatty acids (MUFAs) and readily oxidizable PUFAs, C18:2 and C18:3 in control w^{1118} and TAZ^{889}-deficient flies. **d**,**e**, TAZ deficiency results in accumulation of oxygenated (**d**) and oxidatively truncated phospholipids (**e**). Data are presented as mean ± s.d. MLCL(50:4)-OH-OOH, $^{**}P = 0.0069$; PE(36:2)-OOH, $^{*}P = 0.0190$; PCp(34:2)-OOH, $^{*}P = 0.0112$; MLCL(16:1/16:1/ONA), $^{**}P = 0.0087$; PE(16:1)-ONA, $^{*}P = 0.0215$, unpaired *t*-test. **f**, TPP–IOA improves the endurance of TAZ^{889} mutants. Each vial of 20 flies was treated statistically as a single independent replicate ($n = 8$ biological replicates for each group). Significance was determined by log-rank analysis. Age at day 10, *P* value for 0.89 mg ml^{-1} = 0.0097, *P* value for 1.78 mg ml^{-1} = 0.0257. Age at day 17, *P* value for 0.89 mg ml^{-1} = 0.0032, *P* value for 1.78 mg ml^{-1} < 0.0001. In graph, $^{**}P < 0.01$, $^{****}P < 0.0001$. **g**, Content of CL (left) and MLCL (right) in TAZ^{889}-deficient flies after feeding TPP–IOA. Data are presented as mean ± s.d. CL, $^{*}P = 0.0121$; MLCL, $^{*}P = 0.0313$, unpaired two-tailed *t*-test. **h**, TPP–IOA protects lipids against oxidation induced by TAZ deficiency. Data are presented as mean ± s.d. One-way ANOVA, Tukey's multiple comparison test. MLCL(50:4)-OH-OOH, $^{*}P = 0.0458$; PE(36:2)-OOH, $^{*}P = 0.0213$; PCp(34:2)-OOH, $^{*}P = 0.0339$, $^{**}P = 0.0032$; MLCL(16:1/16:1/ONA), $^{**}P = 0.0049$ versus TPP–IOA 0.89, $^{**}P = 0.0039$ versus TPP–IOA 1.78; PE(16:1)-ONA, $^{**}P = 0.0022$ versus TPP–IOA 0.89, $^{**}P = 0.0046$ versus TPP–IOA 1.78. Lipidomic analysis was performed using six vials ($n = 20$ fly torsos per vial). For all violin plots presented, individual points including maximal and minimal are shown as black circles. Dashed black line indicates median and dotted lines indicate quartiles.

https://doi.org/10.1038/s42255-023-00926-4

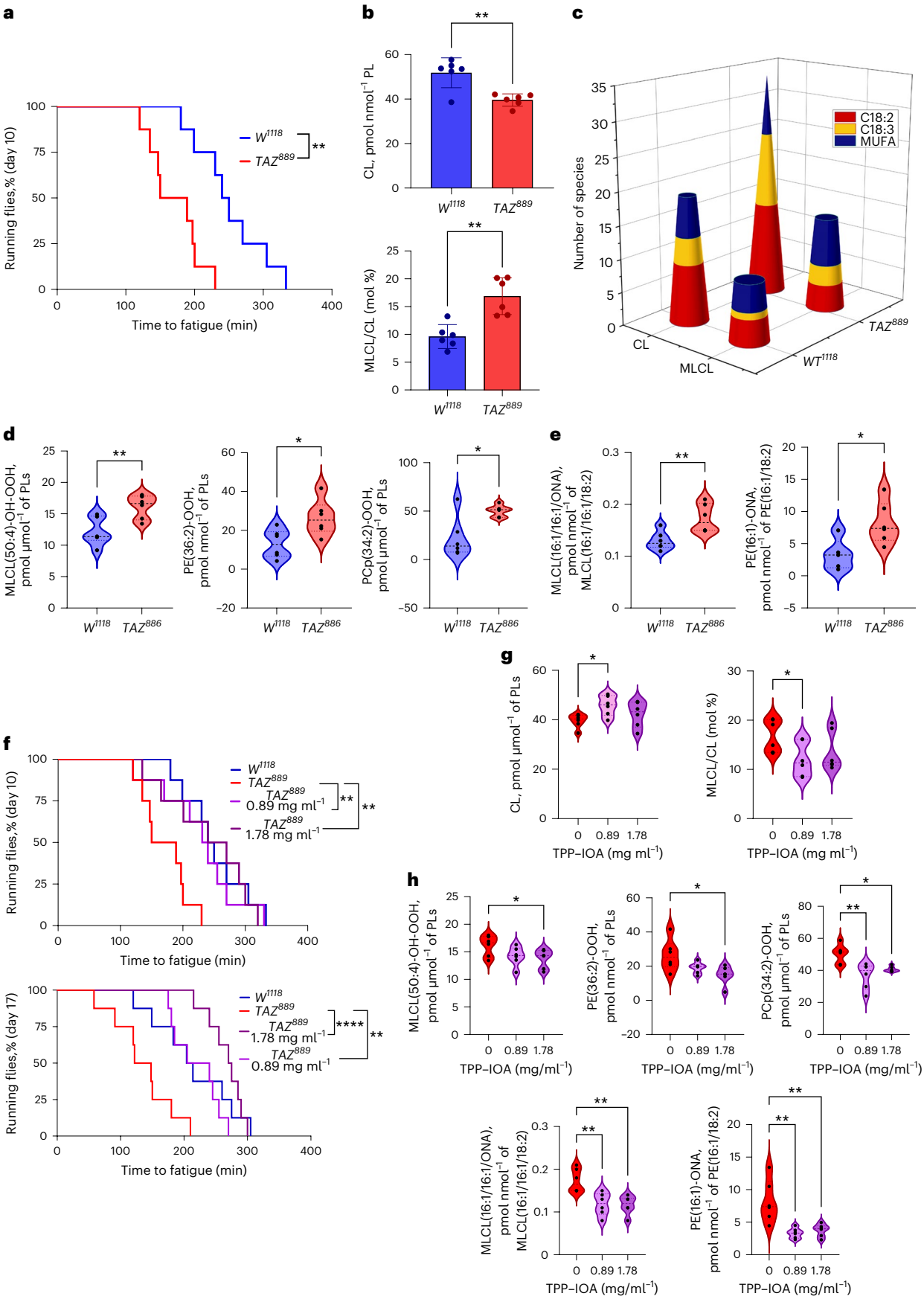

https://doi.org/10.1038/s42255-023-00926-4

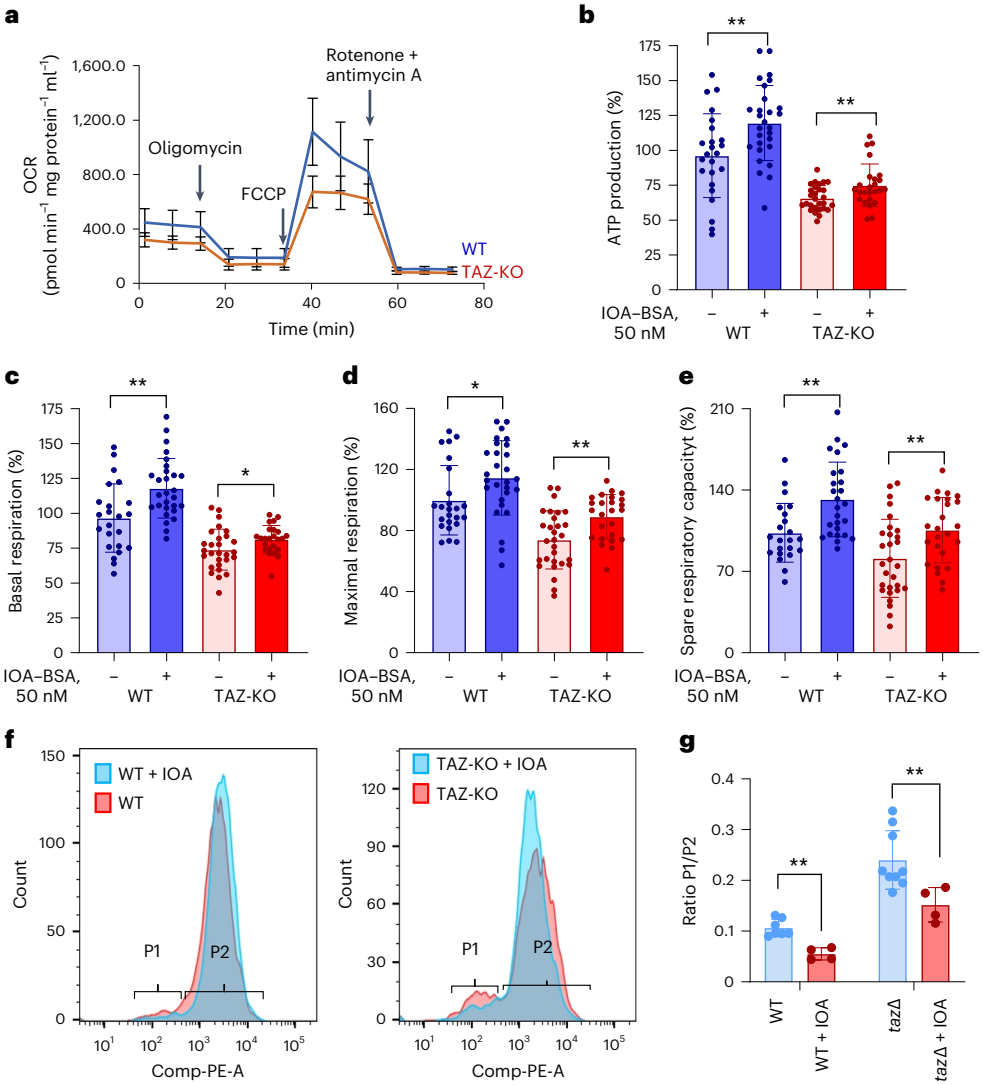

Fig. 7 | Bioenergetic characteristics, mitochondrial membrane potential of WT and TAZ-KO cells and the effect of treatment with MLCL–cyt c peroxidase complex inhibitor IOA. a, Oxygen consumption rate (OCR) assessed by Seahorse XFe96 Extracellular Flux Analyzer in WT and TAZ-KO C2C12 myoblasts. **b**, ATP-linked respiration (ATP production), represented by a decrease in OCR following inhibition of ATP synthase by oligomycin, was lower in TAZ-KO versus WT cells ($P < 0.0001$). IOA increased ATP production in WT and TAZ-KO cells versus respective untreated cells. **c**, Compared to WT, TAZ-KO cells had significantly lower basal respiration ($P = 0.0201$) measured before the addition of the ATP synthase inhibitor, oligomycin. IOA increased basal respiration in WT and TAZ-KO cells versus respective untreated cells. **d**, Maximal respiration measured after the addition of the uncoupler carbonyl cyanide-p-trifluoromethoxyphenyl-hydrazone (FCCP) was decreased in TAZ-KO cells versus WT ($P < 0.0001$). IOA increased maximal respiration in WT and TAZ-KO cells versus respective untreated cells. **e**, Spare respiratory capacity calculated as the difference between maximal respiration and ATP-linked respiration was diminished in TAZ-KO versus WT cells ($P = 0.0055$). IOA improved spare respiratory capacity in WT and TAZ-KO cells versus their untreated counterparts. Data are presented as mean ± s.d. $^{*}P < 0.05$, $^{**}P < 0.01$, two-tailed unpaired *t*-test, between untreated and treated cells from the same group (WT and TAZ-KO); two-way ANOVA followed by Šídák's multiple comparisons test for comparisons between WT and TAZ-KO untreated cells (adjusted *P* values); **a**, *n* = at least 12 biological replicates (microplate wells seeded with 5,000 cells) from one experiment, 12 OCR readings over time for each well, three reading repeats at each point; **b**–**e**, *n* = at least 24 biological independent samples (microplate wells seeded each with 5,000 cells) from two independent experiments, 12 OCR readings over time for each well, three reading repeats at each point. Each data point is the average of 3 × 3 = 9 readings. OCR values were normalized by the protein content of each well independently and then expressed as a percentage of the mean of at least 25 WT wells with no treatment. **f**, Effect of IOA (1 µM) on mitochondrial membrane potential in WT and TAZ-KO C2C12 cells assessed by TMRM. **g**, Quantification was performed using percentage of cells in populations P1 and P2. Data are presented as mean ± s.d. Each data point represents a biologically independent sample. Statistical significance was analyzed using unpaired two-tailed *t*-test. $^{**}P = 0.0018$ (WT versus WT + IOA), $^{**}P = 0.028$ (*tazΔ* versus *tazΔ* + IOA).

effectively propagate the peroxidation reaction without any additional supplementation with H_2O_2.

We demonstrated that MLCL-induced changes in cyt c dynamics are accompanied by rupture of the Fe–S–M_{80} bond. This promotes the transition of the heme–Fe to a penta-coordinated, high-spin configuration that permits access of H_2O_2 and other hydroperoxides (including hydroperoxy-lipids) to the heme catalytic site[47,48]. ssNMR results and computational MD simulations support the dynamic structural impact of MLCL binding, most notably mobilization of the M_{80}-containing Ω-loop of cyt c. Formation of MLCL–cyt c complexes with anomalous peroxidase activity leads to toxic phospholipid peroxidation compatible with two specific features of TAZ deficiency established by redox lipidomics: (1) molecular diversification of MLCL and CL with the appearance of readily oxidizable PUFA species, and (2) accumulation of peroxidation products, including primary hydroperoxy derivatives and secondary oxidatively truncated

degradation products. Formation and accumulation of MLCL and CL peroxidation products in which the hydrophobic acyl chains contain polar oxygen functionalities disrupt normal hydrophobic interactions within the membrane. Furthermore, oxidatively truncated CL and MLCL species covalently modify mitochondrial proteins causing their 'lipoxidation'[49,50].

Not only does MLCL accumulate in TAZ-deficient cells, but its localization also differs from that of CL in WT cells, making it more readily accessible to form peroxidase complexes with cyt c. Given the location of TAZ on the outer leaflet of the IMM, it is assumed that CL must be flipped from the inner leaflet of the IMM (where it is synthesized) to the outer leaflet to undergo remodeling by TAZ[51,52]. The absence of functional TAZ may preclude further translocation of its substrate, MLCL, away from the site where it is typically processed. This suggests that in TAZ-deficient cells, MLCL may accumulate in the outer leaflet of the IMM, immediately adjacent to the location of cyt c in the IMS. In contrast, CL is thought to be enriched in the inner leaflet of the IMM, facing away from cyt c[53]. Moreover, previous work has shown that MLCL is not as potent as CL in binding to mitochondrial membrane protein complexes[54,55]. One implication of such a reduced binding affinity is that MLCL would be more freely available in the IMM (unlike CL that is mostly sequestered within mitochondrial protein complexes). The increased amount of unbound MLCL contributes to destabilization of the IMM, facilitating enhanced lipid scrambling due to increased dynamic disorder as detected also by our ^{31}P ssNMR measurements.

Our study shows that one of the primary substrates of MLCL–cyt c peroxidase complexes is CL, yielding peroxidized CL molecules (CLox). CLox species have been identified as apoptosis cell death signals[17] and production of CLox has been shown to disrupt multiple cellular pathways/functions. For example, CL in the IMM binds and stabilizes respiratory chain complexes, but when CL becomes oxidized, this interaction is diminished, resulting in a concomitant reduction in respiratory chain function[56]. Similarly, increased levels of CLox have been shown to disrupt other fundamental mitochondrial parameters that have been implicated in BTHS pathology, including regulation of cyt c-mediated apoptosis, mitochondrial membrane potential and structure[57–59].

TAZ deficiency associated peroxidation (catalyzed by the MLCL–cyt c peroxidase) is not limited to CL and MLCL but also affects other mitochondrial PUFA phospholipids, including PE, PC, PI and PG. Comparison of the oxidized PUFA phospholipid profiles in BTHS versus control cells showed that: (1) in human lymphoblasts, which contain a limited number of mitochondria, only 8 out of 17 oxygenated phospholipid species were represented by oxidized MLCL and CL species; and (2) in human heart where myocytes are enriched with mitochondria, 20 out of 27 oxygenated species were represented by oxidized MLCL and CL species. Notably, in a model system, while oxygenated species of PUFA-PE and PUFA-PC were formed in PUFA-MLCL–cyt c catalyzed reaction, oxidative metabolites of PUFA-MLCL were predominant. When PUFA-MLCL(L)$_3$ was substituted with non-oxidizable MLCL(O)$_3$, the oxidation of PUFA-PE and PUFA-PC was significantly increased. Thus, MLCL–cyt c complexes formed in BTHS mitochondria can oxidize not only MLCL and CL but also other membrane PUFA phospholipids. Oxygenated phospholipids and their downstream degradation products modulate a host of cellular functions/pathways implicated in BTHS pathology.

Mitochondria damaged by oxidatively modified phospholipids are usually eliminated by mitophagy in which externalization of CL to the mitochondrial surface plays a prominent role[60]. The pool of 'free' CL, markedly depleted by TAZ deficiency, may be insufficient for the fulfillment of this essential signaling function, resulting in the observed defective mitophagy[61,62] and documented by massive enlargement of lysosomes and accumulation of autophagic vacuoles wrapped by mitochondria in hearts of TAZ-deficient mice[62]. In line with this, our data revealed elevated levels of endolysosomal phospholipid biomarkers, BMP[29] in TAZ-deficient C2C12 myoblasts. Of note, enhanced biosynthesis of BMP was observed in lymphoblasts of BTHS patients[63]. Failure to eliminate damaged mitochondria in an attempt to rescue TAZ-deficient cells may prompt regulated death pathways, particularly apoptosis, as has been described in TAZ-deficient mice[64]. This may be further enhanced by high levels of MLCL known to interact with pro-apoptotic tBID[65].

Tissue specificity for the proposed peroxidation mechanism likely results from two factors: (1) tissue-based differences in mitochondrial abundance and expression of TAZ[66], and (2) the relative diversity/abundance of PUFA phospholipids in various tissues. The highest levels of TAZ expression are normally seen in cardiac/skeletal tissue, bone marrow, spleen and brain[66], which can translate into more MLCL species in these tissues as a result of TAZ deficiency. The MLCL:CL ratio is both significantly increased and diversified in a tissue-specific manner in cells from patients with BTHS relative to control cells (0–0.2 in control cells versus 0.4–100 in BTHS patient cells)[54,67]. Therefore, accumulation of peroxidation products would also differ among tissue types and thus cause tissue-selective responses to the MLCL–cyt c activity seen in BTHS. This indicates that generation of MLCL–cyt c complexes can lead to tissue-specific responses in BTHS.

Given the very high level of phospholipid polyunsaturation in the brain, one may suggest that TAZ deficiency should have neurological consequences. Indeed, robust accumulation of CL–MLCL metabolites along with significant memory deficiency has been observed in the brain of TAZ-KO mice[68]. Moreover, several studies have demonstrated major neuropsychological and neurophysiological phenotypes in patients with BTHS, including difficulties in sensory perception, fatigue and cognitive and psychological challenges[69,70]. Patients with BTHS exhibit specific cognitive phenotypes such as lower visual spatial skills and impaired mathematical ability. Moreover, mathematical weakness seems to worsen with age[71,72].

There are several models of BTHS. Although each model has unique characteristics, all models show mitochondrial dysfunction. Homozygous flies lacking full length TAZ transcripts exhibit mitochondrial cristae abnormalities and a nearly 80% reduction in CL levels, similar to that observed in patients with BTHS[31]. As observed in BTHS cells, CL and MLCL in the *Drosophila* BTHS model are represented by oxidizable PUFA phospholipids with two and three double bonds. In addition, the TAZ-deficient *Drosophila* model is characterized by pronounced motor weakness and reduced endurance, two of the most impactful clinical phenotypes reported by patients with BTHS[73,74]. Using this model, we demonstrated that TPP–IOA was effective in suppressing PUFA phospholipid peroxidation and preventing fatigue.

The nature and specific role of the CL re-acylation machinery is not fully understood. While TAZ is an acyl-CoA-independent acyl transferase[75], acyl-CoA-driven exchange mechanisms are also utilized for CL remodeling, including MLCLAT-1 localized to mitochondria[76], ALCAT-1 localized to ER and mitochondria[77] and mitochondrial trifunctional protein dehydrogenase-hydratase alpha subunit[78]. Expression of ALCAT-1 is associated with oxidative stress and implicated in the mitochondrial etiology of diseases related to mitochondria dysfunction[79]. It has also been suggested that α/β hydrolase domain 2 (*ABHD2*) plays a role in the synthesis, turnover or remodeling of phospholipids, including CL[80]. Therefore, one or more acyl-CoA-dependent acylation mechanisms may be involved in restoration of CL–MLCL content in TPP–IOA-treated TAZ-deficient flies.

Our work established that enhanced lipid peroxidation, initiated by MLCL–cyt c complexation, is characteristic of all models of TAZ deficiency employed in the study and engages all major classes of mitochondrial membrane phospholipids. Notably, lipid peroxidation was determined to be a phenotypic characteristic of the BTHS fly model. The fact that IOA has a protective effect on endurance in TAZ-deficient flies strongly suggests that inhibiting lipid peroxidation leads to an increased capacity of skeletal/cardiac muscle activity and decreased fatigue. This is further supported by our demonstration that physiologically relevant concentrations of IOAs preserve bioenergetic functions of mitochondria in TAZ-deficient C2C12 myoblasts. Notably,

high supra-physiological TPP–IOA concentrations (>5 µM) can perturb oxidative phosphorylation and reduce phosphorylation coupling efficiency in vitro as has been noted in our work and found by others[81–85].

In conclusion, the robust effects of IOA and its mitochondria-targeted derivative TPP–IOA, including mitigation of phospholipid peroxidation and mitochondrial respiration in both in vitro and in vivo models, improved endurance in the in vivo fly model along with mechanistic data showing the striking effectiveness of these compounds in suppressing MLCL–cyt c complex peroxidase activity, strongly support our hypothesis that formation of MLCL–cyt c complexes acts as the primary pathogenic mechanism of BTHS and highlights these molecules as a prototype for new therapies.

Methods

Saccharomyces cerevisiae strains

The *S. cerevisiae* WT, *taz1*Δ and *cyc1*Δ yeast strains used in this study were from the BY4741 genetic background (MATa) obtained from the Invitrogen yeast deletion collection (cat. no. 95401.H2). All mutant strains were authenticated by PCR before performing the experiments. The *taz1*Δ*cyc1*Δ mutant strains were generated through genetic crossing between *taz1*Δ and *cyc1*Δ yeast cells. The resulting *taz1*Δ*cyc1*Δ mutants were further confirmed by PCR. Yeast expression plasmids pYES2-EV (MATa *his3Δ1 leu2Δ0 met15Δ0 ura3Δ0*) (empty vector) and pYES2-desa (MATa *his3Δ1 leu2Δ0 met15Δ0 ura3Δ0*) (containing the *H. brasiliensis* Δ^{12}-desaturase gene) were kind gifts from Dr Gasparovic (Rudjer Boskovic Institute).

Mouse C2C12 myoblasts

The TAZ-KO cell line was generated by CRISPR-mediated inactivation of TAZ in a commercially available mouse C2C12 myoblast cell line (ATCC, cat. no. CRL-1772). Disruption of TAZ exon 1 was validated by PCR and genomic sequencing, and loss of TAZ protein expression was validated by immunoblotting before performing experiments. WT C2C12 cells (from which the TAZ-KO mutant was derived) represent an isogenic control for the TAZ-KO cell line. Generation and validation of the TAZ-KO C2C12 cell line have been previously described[19,24].

Drosophila melanogaster strains

TAZ^{889} flies were generated using CRISPR/Cas-9 mediated genomic editing by homology-dependent repair resulting in deletion of nucleotides 8–896 of the *TAFAZZIN* gene. In place of the deletion, a red fluorescent protein marker was knocked in to track the presence of the mutation during cross schemes. The CRISPR plasmid containing the deletion was injected into a *w*^{1118} background and that progenitor line was assessed next to *TAZ*^{889} as a genetic background control. The line was validated by PCR and genomic sequencing and BLAST results confirmed the deletion and RFP insertion. Generation and validation of the *Drosophila TAZ*^{889} strain have been previously described[74].

Flies were kept on a standard 10% yeast and 10% sugar diet and fed either drug or vehicle food. All experimental flies were males collected within a 72-h period and within 24 h of enclosing (n = 160 per experimental group). Males were used exclusively for these experiments because the automated exercise protocol was optimized for males. When flies were 4 d old they were switched to drug food (1.78 mg ml^{-1} or 0.89 mg ml^{-1}) or vehicle food. Drug food was created by dissolving 8.9 mg TPP–IOA in 1 ml water with 25% ethanol. Dilutions were made from the stock (1:5 and 1:10) to achieve 1.78 mg ml^{-1} and a 0.89 mg ml^{-1} solution. Then, 50 µl of either concentration was dropped onto the surface of the food. Flies were fed drug or vehicle food for a full 5 d and on day 10 their endurance was tested.

Endurance was measured by allowing flies to run, using an automated machine (Power Tower) that stimulates them to run upwards in their vial until exhaustion. A vial was considered fatigued when <20% of the flies were still running upwards in the vial. Sample sizes of eight vials for each cohort were not chosen by power analysis but are consistent with numbers from previous experiments[73,74]. Pair-wise log-rank tests were performed to determine significance.

Data distribution was assumed to be normal but was not formally tested. Vials were scored for fatigue by experimenters who were blinded to the treatment and genotype group.

BTHS lymphoblast cell lines

Three BTHS lymphoblast cell lines (GM22164, GM22150 and GM22129) derived from clinically affected patients and characterized by loss-of-function mutations in TAZ, along with three lymphoblast lines derived from apparently healthy demographic-matched control individuals (AG14840, AG14798 and AG14725) were obtained from the Coriell Institute for Medical Research. These cell lines were validated before submission to the Coriell Institute. The TAZ mutation associated with each BTHS patient cell line is as follows: GM22164, Gln233Ter; GM22150, Trp79Ter; and GM22129, IVS1+5G>A.

Mouse model of BTHS and heart tissue

The mouse experiments were performed with approval of the University of Manitoba Animal Policy and Welfare Committee, which adheres to the principles for biomedical research involving animals developed by the Canadian Council on Animal Care and the Council for International Organizations of Medical Sciences and was reported in accordance with ARRIVE guidelines. The mice strain used was C57BL/6J (animal protocol no. B2019-030/1 (AC11468) from the University of Manitoba). Four-month-old animals were used for all studies and randomized and pooled from separate litters of usually ten per group (WT and TAZ-KD). Sex was considered in the design of the experiments as only male mice with one X chromosome develop TAZ deficiency. Mice were maintained in an environmentally controlled facility (22 °C, 37% humidity and 12-h light–dark cycle) with access to food (diet, TD.01306, Harlan) and water ad libitum. TAZ-deficient animals were generated by mating male transgenic mice (strain B6.Cg-Gt(ROSA)26Sortm1(H1/tetO-RNAi:Taz,CAG-tetR)Bsf/ZkhuJ; The Jackson Laboratory) containing a doxycycline (DOX)-inducible TAZ-specific short-hair-pin RNA (shRNA) with female C57BL/6J mice (The Jackson Laboratory). Knockdown of TAZ was induced in utero by administration of DOX (625 mg of DOX/kg of chow) as part of the standard low-fat 6% (*w*/*w*) DOX-containing rodent chow (Envigo Teklad, Rodent diet, cat. no. TD.01306) to female C57BL/6 mice both before mating and during pregnancy. TAZ deficiency is initiated in utero to maximize the duration of TAZ KD[27]. Dams with litters continued to receive the DOX diet to maintain TAZ knockdown in the offspring for the entire suckling period. Male offspring were then weaned at 3 weeks of age onto the DOX-containing diet. In addition, some dams and corresponding male offspring were fed a low-fat (6%, *w*/*w*) standard rodent chow not treated with DOX and served as standard WT animals. Male mice positive for the TAZ shRNA transgene were identified by PCR using primers (5′-CCATGGAATTCGAACGCTGACGTC-3′ forward and 5′-TATGGGCTATGAACTAATGACCC-3′ reverse). At 4 months of age, hearts from WT and TAZ-KD mice were collected and frozen at −80 °C before analysis. No animals and data points were excluded from the analysis.

Human heart tissue samples

Ascertainment of human myocardial samples was approved by the University of Pittsburgh Institutional Review Board (IRB) protocol STUDY19070300. Patients and patient caregivers provided informed written consent. Discarded human myocardial samples were collected from patients undergoing heart surgery or heart transplantation. In brief, samples were resected from the explanted diseased heart after heart transplantation. Samples from donor hearts that ended up not being used for transplantation were collected without recording of any patient identifiers. In these cases, clinical information was retrieved through an honest broker (approval through IRB-P00000126).

Available clinical and demographic characteristics of the non-failing controls and patients are presented in Extended Data Fig. 5a.

Synthesis of imidazole-substituted fatty acid TPP–IOA

The synthesis of TPP–IOA relied on the ready availability of the naturally occurring fatty acid (9*Z*,12*R*)-(+)-ricinoleic acid. The 12-OH group offered a site for heterocycle substitution on a long-chain fatty acid without having to prepare new starting materials. Briefly, methyl ricinoleic acid was mesylated on the 12-hydroxy group (CH_3SO_2Cl, Et_3N, 4-dimethylaminopyridine (DMAP); CH_2Cl_2, 0 °C to room temperature). The crude mesylates were used without purification as they tended to decompose when chromatographed on silica. Substitution of the mesylate by imidazole could be affected in tetrahydrofuran (THF) solution using potassium *tert*-butoxide and 18-crown-6, but almost identical yields could be obtained by simply heating the mesylates with 2–3 equivalents of imidazole at ~80–90 °C in the absence of solvent. Hydrolysis of the methyl esters with NaOH in a mixture of MeOH/CH_2Cl_2 afforded the free carboxylic acids that could then be esterified with 3-hydroxypropyltriphenylphosphonium bromide (DCC, CH_2Cl_2). Overall yields were about 20% from the starting fatty acid methyl esters. The synthetic scheme for TPP–IOA is shown below.

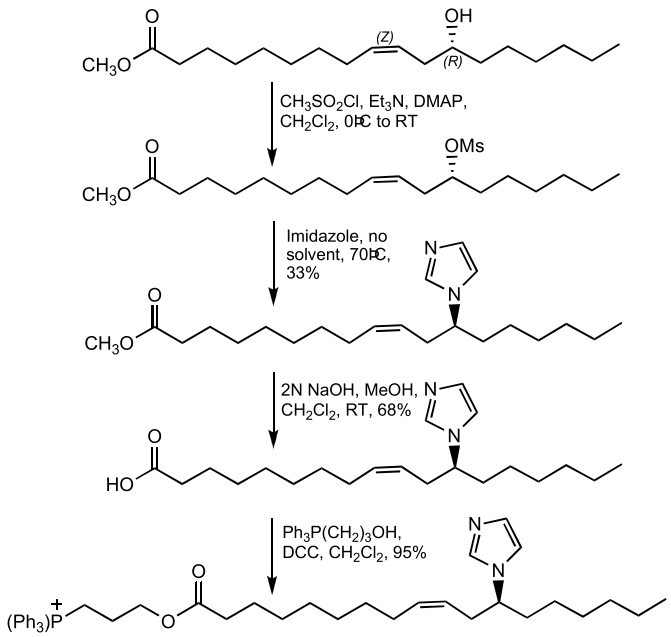

9-(*Z*)-(3-(12-imidazol-1-yl)octadeca-9-enoyloxy)propyl) triphenyl-phosphonium bromide

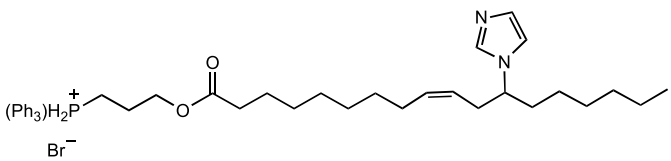

3-Hydroxypropyltriphenylphosphine (876.5 mg, 2.46 mmol), N,N′-dicyclohexylcarbodiimide (485.6 mg, 2.35 mmol) and 12-imidazol-1-yl-(*Z*)-9-octadecaenoate (816.7 mg, 2.34 mmol) were dissolved in 50 ml dichloromethane. The mixture was allowed to stir at room temperature overnight. The mixture was filtered using Celite to remove the precipitated urea and evaporated to provide a crude product that was purified via column chromatography (dichloromethane:methanol, 10:1) to yield 1.54 g (2.23 mmol, 95.3%) of a light yellow, thick oil. R_f = 0.58 (dichloromethane:methanol 10:1). ^{1}H NMR (300 MHz, $CDCl_3$) δ 7.90–7.65 (m, 15H), 7.54 (s, 1H), 7.03 (s, 1H), 6.93 (s, 1H), 5.37 (m, 1H), 5.14 (m, 1H), 4.34 (t, 2H), 3.98 (m, 3H), 2.43 (m, 2H), 2.22 (t, 2H), 1.98 (m, 2H), 1.85–1.72 (m, 4H), 1.51 (m, 2H), 1.25–1.15 (m, 18H), 0.81 (t, 3H); ^{13}C NMR ($CDCl_3$) δ 172.9, 134.82, 134.78, 133.2, 133.1, 133.0, 130.2, 130.0, 128.1, 123.4, 117.9, 116.8, 116.4, 62.7, 62.5, 58.4, 49.4, 34.9, 33.7, 33.6, 31.1, 28.8, 28.6, 28.5, 28.3, 26.7, 25.5, 24.3, 22.0, 21.8, 19.6, 18.9, 13.5; MS (FAB) *m/z* 651 (M+, 100%), 375 (11%), 319 (15%), 303 (12%) and 289 (11%).

Preparation of liposomes

To study the peroxidase activity of cyt c–MLCL complexes, we utilized model systems with liposomes of different phospholipid composition. The three major goals of these experiments were to establish whether: (1) oxidizable PUFA-MLCL in the complex with cyt c are preferred substrates of peroxidation; (2) oxidizable PUFA PLs that do not readily form complexes with MLCL can be peroxidized by cyt c complexes with non-oxidizable MLCL species, and (3) PUFA PLs can be co-oxidized by peroxidase activity of cyt c complexes with PUFA-MLCL. Experimentally, these goals were addressed using three types of liposomes: liposomes of group I contained: DOPC–MLCL(L_3) (2:1 ratio), liposomes of group II contained: DOPC–MLCL($O)_3$–SLPC (2:1:1 ratio), DOPC–MLCL($O)_3$–SLPE, DOPC–MLCL($O)_3$–SAPC (2:1:1 ratio), DOPC–MLCL($O)_3$–SAPE, (2:1:1 ratio), liposomes of group III contained: DOPC–MLCL(L_3)–SLPC (2:1:1 ratio), DOPC–MLCL($L)_3$–SLPE, DOPC–MLCL($L)_3$–SAPC (2:1:1 ratio), DOPC–MLCL($L)_3$–SAPE, DOPC–MLCL($L)_3$–MLCL($O)_3$–SAPC (2:1:1:1 ratio) and DOPC–MLCL($L)_3$–MLCL($O)_3$–SAPE (2:1:1:1 ratio). All liposomes were prepared by extrusion through a membrane with 100-nm pores in 25 mM HEPES buffer (pH 7.4) to a concentration of 100 μM in DTPA using a mini-extruder (Avanti Polar Lipids). Liposomes (100 μM) were incubated in the presence of cyt c (10 μM) and H_2O_2 (25 μM was added every 10 min) at 37 °C. At the end of incubation, lipids were extracted and analyzed by LC–MS.

Absorption spectroscopy

Optical spectra were recorded using a UV160U spectrophotometer (Shimadzu). Samples in 25 mM HEPES buffer (pH 7.4) 100 μM in DTPA were contained in a 50-μl cuvette with 0.3-mm path length. The final concentration of cyt c in the experiments was 75 μM. Incubations were performed at room temperature. IOA and TPP–IOA dissolved in dimethylsulfoxide (DMSO) were added in ratios of IOA–cyt c of 2:1 and 4:1. Cyt c was pre-incubated with IOA for 10 min before addition of liposomes. The baseline was subtracted from each individual spectrum before obtaining the differential spectra to minimize the interference of light scattering. For assessment of the formation of high-spin iron we calculated the absorbance at 620 nm by subtraction of the absorbance reading at 675 nm from the absorbance reading at 620 nm.

Oxidation of BODIPY-C11 by cyt c–MLCL

Cyt c (2 μM) was mixed with DOPC–MLCL liposomes containing bovine heart MLCL consisting of 90% MLCL($L)_3$ or MLCL($O)_3$ (MLCL–cyt c ratio of 20:1) and incubated with BODIPY-C11 (1 μM) and H_2O_2 (25 μM) in 25 mM HEPES buffer (pH 7.4) containing 100 μM DTPA. An imaging reader Cytation 5 and UV160U spectrophotometer (Shimadzu) were used to measure fluorescence of BODIPY-C11 and record its spectra at emission wavelength 515 nm after excitation at 495 nm, respectively.

WT, *taz1*Δ, *cyc1*Δ and *taz1*Δ*cyc1*Δ (n = 4) yeast cells were grown overnight to the mid log phase. Cells (OD 1.0) were washed with PBS twice, stained with 2 μM BODIPY-C11 (Thermo Fisher Scientific) in PBS, treated with 50 μM tBHP (Millipore-Sigma) and incubated at 30 °C for 30 min. Fluorescence intensity was measured using flow cytometry (Cytek Northern Lights) at the Microscopy, Imaging and Cytometry Resources Core, Wayne State University, School of Medicine. Median fluorescence intensity of single cells was analyzed by FlowJo software v.10. No statistical methods were used to predetermine sample sizes, but a sample size of three to four biological replicates has been deemed sufficient for statistical analysis of most flow cytometry data[86]. The gaiting strategy is presented on Supplementary Fig. 1. Data distribution was assumed to be normal but this was not formally tested. Data

collection and analysis were not performed blind to the conditions of the experiments.

Mitochondrial bioenergetics

WT and TAZ-KO C2C12 cells were seeded in six-well plates (150,000 cells per well) and treated with IOA (50 nM) in complete DMEM for 2 d. To prevent possible toxicity of IOA, it was delivered to cells as a complex with fatty-acid-free albumin (IOA:BSA, 3:1), which was used in all incubations and assessments of bioenergetic parameters. Cells were then collected and plated in a 96-well Seahorse assay plate (5,000 cells per well) and drug treatment was continued for an additional 3 d. On the day of the assay, medium was removed and cells were treated with fresh 1 µM IOA solution in complete DMEM for 4 h. Controls were subjected to the same procedures with drug-free medium. For the Seahorse assay on day 5, complete DMEM was removed, cells (experimental and controls) were washed with XF DMEM assay medium without drug and incubated for 1 h in a non-CO_2 incubator. OCR was measured in accordance with the XF Cell Mito Stress Test kit protocol in a Seahorse XFe96 Extracellular Flux Analyzer. All media were devoid of pyruvate and contained glucose and L-glutamine as energy sources. Complete DMEM also contained 10% fetal bovine serum and antibiotics (penicillin + streptomycin). Two independent experiments were performed with at least 24 biological replicates (microplate wells seeded each with 5,000 cells). For each well, there were 12 OCR readings over time, with three reading repeats at each of these 12 points. OCR values were normalized by the protein content of each well independently and then expressed as a percentage of the mean of at least 25 WT wells with no treatment.

Mitochondrial membrane potential

WT and TAZ-KO C2C12 cells were seeded in 24-well plates and grown in medium with or without IOA (1 µM) in the presence of fatty-acid-free BSA (IOA:BSA, 3:1) for 3 d. On the day of the experiment, cells were detached by trypsinization, resuspended in DMEM without fetal bovine serum and incubated in a CO_2 incubator with 100 nM TMRM for 30 min. Cells were then washed once with DMEM and resuspended in 500 µl DMEM without fetal bovine serum. Cells were analyzed using a BD FACSCanto flow cytometer with excitation at 488 nm and an emission filter at 585 ± 42 nm (PE equivalent bandpass filter).

Redox phospholipidomics

Lipids were extracted using the Folch procedure and phosphorus was determined by a micro-method. PLs were analyzed by LC–MS using a Dionex Ultimate 3000 HPLC system coupled on-line to an Orbitrap Fusion Lumos mass spectrometer (Thermo Fisher) using a normal phase column (Luna 3 µm Silica (2) 100 Å, 150 × 2.0 mm (Phenomenex)). The analysis was performed using gradient solvents (A and B) containing 10 mM ammonium formate at a flow rate of 0.2 ml min^{-1}. Solvent A contained isopropanol/hexane/water (285:215:5, *v*/*v*/*v*) and solvent B contained isopropanol/hexane/water (285:215:40, *v*/*v*/*v*). The column was eluted for 0–23 min with a linear gradient from 10% to 32% B; 23–32 min with a linear gradient of 32–65% B; 32–35 min with a linear gradient of 65–100% B; 35–62 min held at 100% B; 62–64 min with a linear gradient from 100% to 10% B; followed by an equilibration from 64–80 min at 10% B. Analysis was performed in negative-ion mode at a resolution of 140,000 for the full MS scan in a data-dependent mode. Analysis of raw LC–MS data was performed using software package Compound Discoverer 2.1 (Thermo Fisher) with an in-house generated analysis workflow and oxidized PL database. Briefly, peaks with S/N ratio >3 were identified and searched against oxidized phospholipid database. Lipids were further filtered by retention time and confirmed by a fragmentation mass spectrum. Deuterated phospholipids (Avanti Polar Lipids) were used as internal standards. Values for *m*/*z* were matched within 5 ppm to identify the lipid species. All samples were analyzed randomly.

EPR measurements of peroxidase activity

EPR spectra of *N*-benzyl-*N*-(*tert*-butyl)nitroxide were recorded at room temperature in gas-permeable Teflon tubing (inner diameter, 0.8-mm; thickness, 0.013; Alpha Wire) on a JES-FA 100 ESR spectrometer (JEOL) at X-band (9.4 GHz). The tubing (length, 20 cm) was filled with a 90-µl sample, double-folded and placed in an open 3.0-mm (internal diameter) EPR quartz tube. The spectra were recorded under the following EPR conditions: center field, 335.08 mT; sweep width, 5 mT; microwave power, 10 mW; width modulation, 0.06 mT; time constant, 0.03 s; and scan time, 30 s. The magnitude of the EPR signal of *N*-benzyl-*N*-(*tert*-butyl)nitroxide was measured 1 min after the addition of 20 µM H_2O_2 to the 5 µM cyt c, 100 µM phospholipid and 100 µM *N*-benzyl-*N*-(*tert*-butyl)hydroxylamine in buffer solution (25 mM HEPES buffer, pH 7.4). Concentration of (Z)-12-(1H-imidazol-1-yl) octadec-9-enoic acid (IOFA) was 10 µM (phospholipid/IOFA–cyt c (20:2:1)).

Protein production, liposome preparation and solid-state NMR measurements

Human cyt c was produced in *E. coli* BL21 (DE3) cells using the pBTR-1 plasmid (AddGene plasmid #22468), which consists of the *CYCS* and *CYC3* genes, coding for human cyt c and yeast cyt c heme lyase, where the latter is needed for the correct heme integration in c-type cytochromes[87]. Uniformly ^{13}C, ^{15}N enriched cyt c was produced according to previously described protocols[87]. Cells were grown in minimal medium containing 0.1% (*w*/*v*) $^{15}NH_4Cl$ and 0.4% (*w*/*v*) ^{13}C D-glucose, 50 µM $FeCl_3$ and 100 µM unlabeled δ-aminolevulinic acid. Briefly, protein purification was conducted using a HiTrap SP HP ion exchange chromatography column equilibrated with 20 mM sodium borate, pH 8.5. Protein elution was performed with 1 M NaCl. HPLC–ESI-MS analysis was used to confirm the intact molecular mass of the obtained protein. Oxidized cyt c was obtained by addition of a fivefold molar excess of $K_3Fe(CN)_6$ in 20 mM HEPES (pH 7.4) at room temperature for 20 min, followed by buffer exchange into 20 mM HEPES (pH 7.4) using Amicon ultracentrifugation filters with a 3-kDa cutoff. Protein concentration and completion of oxidation were determined by UV-vis spectrophotometry analysis based on known molar extinction coefficients[88]. DOPC (C18:1), bovine heart MLCL and bovine heart CL were purchased from Avanti Polar Lipids.

Mixtures of MLCL–DOPC or CL–DOPC PLs were used to prepare unilamellar liposomes by extrusion[88]. Stocks of PLs in chloroform were mixed in a 1:1 (or 1:2) molar ratio, dried under N_2 gas and placed under vacuum overnight. The dried lipid films were resuspended in 20 mM HEPES buffer (pH 7.4), vortexed and exposed to five freeze–thaw cycles at −78 °C (liquid nitrogen bath) and 56 °C (water bath). Finally, the lipid solutions were extruded using an Avanti mini-extruder through 200 nm polycarbonate membrane 21 times, to obtain large unilamellar vesicles (LUVs). LUVs were slowly added into cyt c stock solution to a final 1:25 P:L (protein-to-lipid) molar ratio. The resulting suspension was incubated and vortexed for ~15 min at room temperature. The protein–lipid complexes were transferred into 3.2-mm regular-wall MAS ssNMR rotors using a home-built packing tool[89] via an ultracentrifugation step at 175,000*g*, for 3 h at 4 °C (Optima L-100 XP ultracentrifuge with a SW-32 Ti rotor, Beckman Coulter). The same procedure was followed to prepare cyt c–MLCL-containing liposomes complexes (1:40 P:L molar ratio) with and without the IOA inhibitor. IOA was added to the protein in a fourfold molar excess before binding to the lipids, and MLCL/DOPC PLs were mixed in a 1:2 molar ratio.

The ssNMR measurements were performed on an AVANCE NEO 600 MHz (14.1 T) spectrometer from Bruker Biospin. The 2D ^{13}C-^{13}C cross polarization (CP) dipolar-assisted rotational resonance (DARR) solid-state NMR spectra were acquired using a 3.2-mm Bruker EFree HCN MAS probe, at 10 kHz MAS and 253 K temperature. A 70–100% ramped ^{1}H–^{13}C CP step, 25-ms DARR ^{13}C–^{13}C mixing and 5 µs 90° carbon pulse and 2.5 µs 90° proton pulse were used. Two-pulse

phase-modulated (TPPM) proton decoupling during acquisition was around 83 kHz, recycle delay set to 2.7 s and number of scans 64 per data point. The 2D ^{15}N-^{13}C NCA spectra were acquired at 10 kHz MAS and 253 K temperature, using 100 kHz TPPM proton decoupling, 3 s recycle delay and 256 scans per data point. Here, the first step was a CP-MAS transfer from ^{1}H to ^{15}N with a 70–100% ramp on ^{1}H, using rf fields of approximately 75 (^{1}H) and 50 (^{15}N) kHz and an optimized contact time of 1 ms. The magnetization was transferred from ^{15}N to ^{13}C in a second CP step using a 90–100% ramp on ^{13}C, and selectivity was achieved by setting the carrier frequency to be on-resonance with Cα and with an optimized contact time of 5 ms. A 2D grid search was used to optimize the power level of the ^{13}C and ^{15}N channels. The 2D ^{13}C–^{13}C spectra to detect the highly mobile carbons were obtained by combining refocused INEPT ^{1}H–^{13}C transfers with the P9$^{1}_{3}$ total through bond correlation spectroscopy (TOBSY) pulse sequence at 10 kHz MAS and 278 K[22]. ^{1}H decoupling around 70 kHz was applied during evolution and acquisition, 2.5 s recycle delay and 64 scans per data point were used. The 1D ^{13}C direct excitation, INEPT and CP spectra were measured using 50 kHz ^{13}C nutation frequency, 2.5 s repetition delay, 512 scans, 0.015 s acquisition time, 10 kHz spinning frequency and temperature set to 278 K. During the acquisition time, proton TPPM decoupling was set at 83 kHz. ^{13}C-^{1}H 70–100 ramped MAS CP experiment was conducted using 1 ms contact time. The ssNMR spectra were processed and peaks were integrated with the NMRPipe software package[90]. Chemical shifts were indirectly referenced to 4,4-dimethyl-4-silapentane-1 sulfonic acid and liquid ammonia using adamantane ^{13}C chemical shifts as an external reference[88]. NMR spectral analysis and peak assignment were performed in the CcpNmr software suite v.2.4 and NMRPipe software tools[88,90]. The molecular structure of cyt c was visualized using the UCSF Chimera program[91].

Computational methods

Molecular dynamics simulations and molecular docking. Full-atomic MD simulations of horse heart cytochrome c structure (PDB code 1hrc (ref. 92) were performed in the presence of membrane, containing 50% DOPC, 30% DOPE and 20% MLCL molecules. The initial system (Supplementary Video 1, initial frame) and inputs were prepared using CHARMM-GUI server[93]. The structure and parameters of the MLCL structure were prepared based on the CL TLCL2 parameters for lipids defined in the CHARMM force field and heme group parameters were obtained from Autenrieth et al.[94]. MD simulations of cyt c were performed using NAMD[95] software. The simulation setup consisted of cyt c placed at a distance of 15 Å from the membrane and solvated with TIP3P water molecules. At the initial stage, we performed 20 independent MD runs for MLCL (100 ns each). Each independent MD run was first energy-minimized using steepest descent algorithm, followed by a short equilibration where the backbone atoms of the protein were restrained and the remaining atoms were allowed to relax for 2.5 ns. This was followed by a production run of 100 ns each at constant temperature of 303 K and a pressure coupling of 1 bar MD systems at 100 ns were sorted based on the binding interface with the membrane. Ten cyt c conformations in which the molecule diffused toward the bilayer and its positively charged amino acids and M_{80} interacted with MLCLs (Extended Data Fig. 2a, labeled in red) were further selected to be extended to 300 ns. In the simulations in which we observed strong interactions between M_{80} and MLCL, and given that the bond between M_{80} and heme–Fe is disturbed upon membrane binding[46], we drastically weakened the Fe–S bond between M_{80} and the catalytic iron and extended simulations up to 950 ns (Extended Data Fig. 3c), which led to a complete rupture of the Fe–S bond.

Apart from the simulations in explicit membrane, we carried out four independent MD runs of cyt c in explicit water, including two in which the Fe–S bond was removed (Extended Data Fig. 3b). Before productive runs, which were 100-ns long, the following protocol was adopted: 0.2 ns of water equilibration, 10,000 steps of minimization, 0.35 ns of heating from 0 to 300 K and 0.15 ns equilibration of the whole system. Simulations were performed with a cutoff of 12 Å for non-bonded interactions and a Langevin piston algorithm to maintain the temperature at 300 K and pressure at 1 atm.

Docking simulations of IOA inhibitor to cyt c were performed using SMINA[96]. Five runs were performed and the one with the lowest binding energy (highest affinity) was selected for further investigation. Among the conformations, we selected the one with the shortest distance between the Fe^{3+} and N atom of imidazole (~3.5 Å). We further performed 200 ns MD simulations (two independent runs) for the cyt c–IOA complex on which we applied temporary restraints between the Fe^{3+} and N atom of IOA imidazole so that the IOA could optimize its interaction with the protein structure. After 200 ns, the restraints were removed and we performed ten additional 300-ns runs for the complex where we could observe stable interactions between the IOA imidazole and the heme group. Non-standard parameters were set based on the default CHARMM ff lipid parameters (for MLCL) and Swiss-param[97] with quantum chemistry calculations. We used and our in-house developed scripts implemented in the ProDy[98] API for trajectory analysis.

Quantification and statistical analysis. Comparisons of means were performed using an unpaired two-tailed Student's *t*-test and one-way ANOVA with Tukey post hoc test. Data are reported as mean ± s.d. unless otherwise stated.

Statistical analyses were performed using GraphPad Prism. SIMCA v.16.1 software (Sartorius) was used to perform OPLS-DA of lipidomes data. The data were presented as an OPLS-DA score plot, an S-plot derived from OPLS-DA that indicates important variables and a VIP score that is a measure of the importance of variables in the OPLS-DA model. A variable with a VIP score close to or >1.2 was considered important in given model.

Reporting summary

Further information on research design is available in the Nature Portfolio Reporting Summary linked to this article.

Data availability

Source data for Figs. 1–7 and Extended Data Figs. 4–8 are provided with the manuscript. Raw flow cytometry data can be accessed from the FlowRepository database (repository ID FR-FCM-Z6XG). MS data are available upon request. Source data are provided with this paper.

Code availability

No custom code was generated for this study.

References

1. Reid Thompson, W. et al. A phase 2/3 randomized clinical trial followed by an open-label extension to evaluate the effectiveness of elamipretide in Barth syndrome, a genetic disorder of mitochondrial cardiolipin metabolism. *Genet. Med.* **23**, 471–478 (2021).
2. Dabner, L. et al. Treatment of Barth syndrome by cardiolipin manipulation (CARDIOMAN) with bezafibrate: protocol for a randomized placebo-controlled pilot trial conducted in the nationally commissioned Barth syndrome service. *JMIR Res. Protoc.* **10**, e22533 (2021).
3. Kagan, V. E., Chu, C. T., Tyurina, Y. Y., Cheikhi, A. & Bayir, H. Cardiolipin asymmetry, oxidation and signaling. *Chem. Phys. Lipids* **179**, 64–69 (2014).
4. Oemer, G. et al. Molecular structural diversity of mitochondrial cardiolipins. *Proc. Natl Acad. Sci. USA* **115**, 4158–4163 (2018).
5. Maguire, J. J. et al. Known unknowns of cardiolipin signaling: the best is yet to come. *Biochim. Biophys. Acta Mol. Cell Biol. Lipids* **1862**, 8–24 (2017).

6. Ren, M., Miller, P. C., Schlame, M. & Phoon, C. K. L. A critical appraisal of the tafazzin knockdown mouse model of Barth syndrome: what have we learned about pathogenesis and potential treatments? *Am. J. Physiol. Heart Circ. Physiol.* **317**, H1183–H1193 (2019).
7. Schlame, M. & Greenberg, M. L. Biosynthesis, remodeling and turnover of mitochondrial cardiolipin. *Biochim. Biophys. Acta Mol. Cell Biol. Lipids* **1862**, 3–7 (2017).
8. Claypool, S. M. & Koehler, C. M. The complexity of cardiolipin in health and disease. *Trends Biochem. Sci.* **37**, 32–41 (2012).
9. Beranek, A. et al. Identification of a cardiolipin-specific phospholipase encoded by the gene CLD1 (YGR110W) in yeast. *J. Biol. Chem.* **284**, 11572–11578 (2009).
10. Sparagna, G. C. & Lesnefsky, E. J. Cardiolipin remodeling in the heart. *J. Cardiovasc. Pharmacol.* **53**, 290–301 (2009).
11. Ji, J. & Greenberg, M. L. Cardiolipin function in the yeast S. cerevisiae and the lessons learned for Barth syndrome. *J. Inherit. Metab. Dis.* **45**, 60–71 (2022).
12. Li, M. et al. Activation of cytochrome C peroxidase function through coordinated foldon loop dynamics upon interaction with anionic lipids. *J. Mol. Biol.* **433**, 167057 (2021).
13. Li, M. et al. Surface-binding to cardiolipin nanodomains triggers cytochrome c pro-apoptotic peroxidase activity via localized dynamics. *Structure* **27**, 806–815 (2019).
14. Baile, M. G., Whited, K. & Claypool, S. M. Deacylation on the matrix side of the mitochondrial inner membrane regulates cardiolipin remodeling. *Mol. Biol. Cell* **24**, 2008–2020 (2013).
15. Tuominen, E. K., Wallace, C. J. & Kinnunen, P. K. Phospholipid-cytochrome c interaction: evidence for the extended lipid anchorage. *J. Biol. Chem.* **277**, 8822–8826 (2002).
16. Nantes, I. L., Zucchi, M. R., Nascimento, O. R. & Faljoni-Alario, A. Effect of heme iron valence state on the conformation of cytochrome c and its association with membrane interfaces. A CD and EPR investigation. *J. Biol. Chem.* **276**, 153–158 (2001).
17. Kagan, V. E. et al. Cytochrome c acts as a cardiolipin oxygenase required for release of proapoptotic factors. *Nat. Chem. Biol.* **1**, 223–232 (2005).
18. Battistuzzi, G. et al. Role of Met80 and Tyr67 in the low-pH conformational equilibria of cytochrome c. *Biochemistry* **51**, 5967–5978 (2012).
19. Li, Y. et al. Cardiolipin-induced activation of pyruvate dehydrogenase links mitochondrial lipid biosynthesis to TCA cycle function. *J. Biol. Chem.* **294**, 11568–11578 (2019).
20. Imai, M. et al. Investigation of the redox-dependent modulation of structure and dynamics in human cytochrome c. *Biochem. Biophys. Res. Commun.* **469**, 978–984 (2016).
21. Matlahov, I. & van der Wel, P. C. A. Hidden motions and motion-induced invisibility: dynamics-based spectral editing in solid-state NMR. *Methods* **148**, 123–135 (2018).
22. Andronesi, O. C. et al. Determination of membrane protein structure and dynamics by magic-angle-spinning solid-state NMR spectroscopy. *J. Am. Chem. Soc.* **127**, 12965–12974 (2005).
23. Powell, G. L. & Marsh, D. Polymorphic phase behavior of cardiolipin derivatives studied by 31P NMR and X-ray diffraction. *Biochemistry* **24**, 2902–2908 (1985).
24. Lou, W. et al. Genetic re-engineering of polyunsaturated phospholipid profile of Saccharomyces cerevisiae identifies a novel role for Cld1 in mitigating the effects of cardiolipin peroxidation. *Biochim. Biophys. Acta Mol. Cell Biol. Lipids* **1863**, 1354–1368 (2018).
25. Horvath, S. E. & Daum, G. Lipids of mitochondria. *Prog. Lipid Res.* **52**, 590–614 (2013).
26. Lou, W. et al. Loss of tafazzin results in decreased myoblast differentiation in C2C12 cells: a myoblast model of Barth syndrome and cardiolipin deficiency. *Biochim. Biophys. Acta Mol. Cell Biol. Lipids* **1863**, 857–865 (2018).
27. Acehan, D. et al. Cardiac and skeletal muscle defects in a mouse model of human Barth syndrome. *J. Biol. Chem.* **286**, 899–908 (2011).
28. Kobayashi, T. et al. A lipid associated with the antiphospholipid syndrome regulates endosome structure and function. *Nature* **392**, 193–197 (1998).
29. Showalter, M. R. et al. The emerging and diverse roles of bis(monoacylglycero) phosphate lipids in cellular physiology and disease. *Int. J. Mol. Sci.* **21**, 8067 (2020).
30. Atkinson, J. et al. A mitochondria-targeted inhibitor of cytochrome c peroxidase mitigates radiation-induced death. *Nat. Commun.* **2**, 497 (2011).
31. Xu, Y. et al. A *Drosophila* model of Barth syndrome. *Proc. Natl Acad. Sci. USA* **103**, 11584–11588 (2006).
32. Malhotra, A. et al. Role of calcium-independent phospholipase A2 in the pathogenesis of Barth syndrome. *Proc. Natl Acad. Sci. USA* **106**, 2337–2341 (2009).
33. Creed, S. & McKenzie, M. Measurement of mitochondrial membrane potential with the fluorescent dye tetramethylrhodamine methyl ester (TMRM). *Methods Mol. Biol.* **1928**, 69–76 (2019).
34. Pang, J., Bao, Y., Mitchell-Silbaugh, K., Veevers, J. & Fang, X. Barth syndrome cardiomyopathy: an update. *Genes* **13**, 656 (2022).
35. Hornby, B. et al. Natural history comparison study to assess the efficacy of elamipretide in patients with Barth syndrome. *Orphanet. J. Rare Dis.* **17**, 336 (2022).
36. Scott, R. A. & Mauk, A. G. *Cytochrome c: A Multidisciplinary Approach*. (University Science Books, 1996).
37. Alvarez-Paggi, D. et al. Multifunctional cytochrome c: learning new tricks from an old dog. *Chem. Rev.* **117**, 13382–13460 (2017).
38. Kagan, V. E. et al. Cytochrome c/cardiolipin relations in mitochondria: a kiss of death. *Free Radic. Biol. Med* **46**, 1439–1453 (2009).
39. Pinheiro, T. J. & Watts, A. Lipid specificity in the interaction of cytochrome c with anionic phospholipid bilayers revealed by solid-state 31P NMR. *Biochemistry* **33**, 2451–2458 (1994).
40. Cassina, A. M. et al. Cytochrome c nitration by peroxynitrite. *J. Biol. Chem.* **275**, 21409–21415 (2000).
41. Hannibal, L. et al. Alternative conformations of cytochrome c: structure, function, and detection. *Biochemistry* **55**, 407–428 (2016).
42. Schweitzer-Stenner, R. Relating the multi-functionality of cytochrome c to membrane binding and structural conversion. *Biophys. Rev.* **10**, 1151–1185 (2018).
43. Droghetti, E., Oellerich, S., Hildebrandt, P. & Smulevich, G. Heme coordination states of unfolded ferrous cytochrome C. *Biophys. J.* **91**, 3022–3031 (2006).
44. Dunford, H. B. & Stillman, J. S. On the function and mechanism of action of peroxidases. *Coord. Chem. Rev.* **19**, 187–251 (1976).
45. Basova, L. V. et al. Cardiolipin switch in mitochondria: shutting off the reduction of cytochrome c and turning on the peroxidase activity. *Biochemistry* **46**, 3423–3434 (2007).
46. Belikova, N. A. et al. Peroxidase activity and structural transitions of cytochrome c bound to cardiolipin-containing membranes. *Biochemistry* **45**, 4998–5009 (2006).
47. Barr, D. P. & Mason, R. P. Mechanism of radical production from the reaction of cytochrome c with organic hydroperoxides. An ESR spin trapping investigation. *J. Biol. Chem.* **270**, 12709–12716 (1995).
48. Diederix, R. E. et al. Kinetic stability of the peroxidase activity of unfolded cytochrome c: heme degradation and catalyst inactivation by hydrogen peroxide. *Inorg. Chem.* **42**, 7249–7257 (2003).
49. Chicco, A. J. & Sparagna, G. C. Role of cardiolipin alterations in mitochondrial dysfunction and disease. *Am. J. Physiol. Cell Physiol.* **292**, C33–C44 (2007).

50. Amoscato, A. A. et al. Formation of protein adducts with hydroperoxy-PE electrophilic cleavage products during ferroptosis. *Redox Biol.* **63**, 102758 (2023).
51. Claypool, S. M., McCaffery, J. M. & Koehler, C. M. Mitochondrial mislocalization and altered assembly of a cluster of Barth syndrome mutant tafazzins. *J. Cell Biol.* **174**, 379–390 (2006).
52. Schlame, M. Cardiolipin synthesis for the assembly of bacterial and mitochondrial membranes. *J. Lipid Res.* **49**, 1607–1620 (2008).
53. Ge, Y., Boopathy, S., Nguyen, T. H., Lugo, C. M. & Chao, L. H. Absence of cardiolipin from the outer leaflet of a mitochondrial inner membrane mimic restricts Opa1-mediated fusion. *Front. Mol. Biosci.* **8**, 769135 (2021).
54. Duncan, A. L. Monolysocardiolipin (MLCL) interactions with mitochondrial membrane proteins. *Biochem. Soc. Trans.* **48**, 993–1004 (2020).
55. Xu, Y. et al. Loss of protein association causes cardiolipin degradation in Barth syndrome. *Nat. Chem. Biol.* **12**, 641–647 (2016).
56. Musatov, A. Contribution of peroxidized cardiolipin to inactivation of bovine heart cytochrome c oxidase. *Free Radic. Biol. Med* **41**, 238–246 (2006).
57. Petrosillo, G., Casanova, G., Matera, M., Ruggiero, F. M. & Paradies, G. Interaction of peroxidized cardiolipin with rat-heart mitochondrial membranes: induction of permeability transition and cytochrome c release. *FEBS Lett.* **580**, 6311–6316 (2006).
58. Clarke, S. L. et al. Barth syndrome. *Orphanet. J. Rare Dis.* **8**, 23 (2013).
59. Gonzalvez, F. et al. Barth syndrome: cellular compensation of mitochondrial dysfunction and apoptosis inhibition due to changes in cardiolipin remodeling linked to tafazzin (TAZ) gene mutation. *Biochim. Biophys. Acta* **1832**, 1194–1206 (2013).
60. Chu, C. T. et al. Cardiolipin externalization to the outer mitochondrial membrane acts as an elimination signal for mitophagy in neuronal cells. *Nat. Cell Biol.* **15**, 1197–1205 (2013).
61. Zhang, J., Liu, X., Nie, J. & Shi, Y. Restoration of mitophagy ameliorates cardiomyopathy in Barth syndrome. *Autophagy* **18**, 2134–2149 (2022).
62. Hsu, P. et al. Cardiolipin remodeling by TAZ/tafazzin is selectively required for the initiation of mitophagy. *Autophagy* **11**, 643–652 (2015).
63. Hullin-Matsuda, F. et al. De novo biosynthesis of the late endosome lipid, bis(monoacylglycero)phosphate. *J. Lipid Res.* **48**, 1997–2008 (2007).
64. Sohn, J. et al. A new murine model of Barth syndrome neutropenia links TAFAZZIN deficiency to increased ER stress-induced apoptosis. *Blood Adv.* **6**, 2557–2577 (2022).
65. Esposti, M. D., Cristea, I. M., Gaskell, S. J., Nakao, Y. & Dive, C. Proapoptotic Bid binds to monolysocardiolipin, a new molecular connection between mitochondrial membranes and cell death. *Cell Death Differ.* **10**, 1300–1309 (2003).
66. *Human Protein Atlas* https://www.proteinatlas.org/ENSG00000102125-TAZ/tissue
67. Houtkooper, R. H. et al. Cardiolipin and monolysocardiolipin analysis in fibroblasts, lymphocytes, and tissues using high-performance liquid chromatography-mass spectrometry as a diagnostic test for Barth syndrome. *Anal. Biochem.* **387**, 230–237 (2009).
68. Cole, L. K. et al. Aberrant cardiolipin metabolism is associated with cognitive deficiency and hippocampal alteration in tafazzin knockdown mice. *Biochim. Biophys. Acta Mol. Basis Dis.* **1864**, 3353–3367 (2018).
69. Olivar-Villanueva, M., Ren, M. & Phoon, C. K. L. Neurological & psychological aspects of Barth syndrome: clinical manifestations and potential pathogenic mechanisms. *Mitochondrion* **61**, 188–195 (2021).
70. Reynolds, S. Successful management of Barth syndrome: a systematic review highlighting the importance of a flexible and multidisciplinary approach. *J. Multidiscip. Health.* **8**, 345–358 (2015).
71. Raches, D. & Mazzocco, M. M. Emergence and nature of mathematical difficulties in young children with Barth syndrome. *J. Dev. Behav. Pediatr.* **33**, 328–335 (2012).
72. Mazzocco, M. M., Henry, A. E. & Kelly, R. I. Barth syndrome is associated with a cognitive phenotype. *J. Dev. Behav. Pediatr.* **28**, 22–30 (2007).
73. Damschroder, D., Reynolds, C. & Wessells, R. *Drosophila* tafazzin mutants have impaired exercise capacity. *Physiol. Rep.* **6**, e13604 (2018).
74. Damschroder, D. et al. Stimulating the sir2–spargel axis rescues exercise capacity and mitochondrial respiration in a *Drosophila* model of Barth syndrome. *Dis. Model Mech.* **15**, dmm049279 (2022).
75. Schlame, M., Xu, Y. & Ren, M. The basis for acyl specificity in the tafazzin reaction. *J. Biol. Chem.* **292**, 5499–5506 (2017).
76. Taylor, W. A. & Hatch, G. M. Identification of the human mitochondrial linoleoyl-coenzyme A monolysocardiolipin acyltransferase (MLCL AT-1). *J. Biol. Chem.* **284**, 30360–30371 (2009).
77. Rieger, B., Krajcova, A., Duwe, P. & Busch, K. B. ALCAT1 overexpression affects supercomplex formation and increases ROS in respiring mitochondria. *Oxid. Med. Cell Longev.* **2019**, 9186469 (2019).
78. Miklas, J. W. et al. TFPa/HADHA is required for fatty acid β-oxidation and cardiolipin re-modeling in human cardiomyocytes. *Nat. Commun.* **10**, 4671 (2019).
79. Li, J. et al. Cardiolipin remodeling by ALCAT1 links oxidative stress and mitochondrial dysfunction to obesity. *Cell Metab.* **12**, 154–165 (2010).
80. Price, T. R. et al. Lipidomic QTL in Diversity Outbred mice identifies a novel function for α/β hydrolase domain 2 (Abhd2) as an enzyme that metabolizes phosphatidylcholine and cardiolipin. *PLoS Genet.* **19**, e1010713 (2023).
81. Maddalena, L. A., Ghelfi, M., Atkinson, J. & Stuart, J. A. The mitochondria-targeted imidazole substituted oleic acid 'TPP-IOA' affects mitochondrial bioenergetics and its protective efficacy in cells is influenced by cellular dependence on aerobic metabolism. *Biochim. Biophys. Acta Bioenerg.* **1858**, 73–85 (2017).
82. Reily, C. et al. Mitochondrially targeted compounds and their impact on cellular bioenergetics. *Redox Biol.* **1**, 86–93 (2013).
83. Trnka, J., Elkalaf, M. & Andel, M. Lipophilic triphenylphosphonium cations inhibit mitochondrial electron transport chain and induce mitochondrial proton leak. *PLoS ONE* **10**, e0121837 (2015).
84. Di Paola, M. & Lorusso, M. Interaction of free fatty acids with mitochondria: coupling, uncoupling and permeability transition. *Biochim. Biophys. Acta* **1757**, 1330–1337 (2006).
85. Severin, F. F. et al. Penetrating cation/fatty acid anion pair as a mitochondria-targeted protonophore. *Proc. Natl Acad. Sci. USA* **107**, 663–668 (2010).
86. Davis, B. H. et al. Determination of optimal replicate number for validation of imprecision using fluorescence cell-based assays: proposed practical method. *Cytom. B Clin. Cytom.* **84**, 329–337 (2013).
87. Olteanu, A. et al. Stability and apoptotic activity of recombinant human cytochrome c. *Biochem. Biophys. Res. Commun.* **312**, 733–740 (2003).
88. Mandal, A. et al. Structural changes and proapoptotic peroxidase activity of cardiolipin-bound mitochondrial cytochrome c. *Biophys. J.* **109**, 1873–1884 (2015).

89. Mandal, A., Boatz, J. C., Wheeler, T. B. & van der Wel, P. C. A. On the use of ultracentrifugal devices for routine sample preparation in biomolecular magic-angle-spinning NMR. *J. Biomol. NMR* **67**, 165–178 (2017).
90. Delaglio, F. et al. NMRPipe: a multidimensional spectral processing system based on UNIX pipes. *J. Biomol. NMR* **6**, 277–293 (1995).
91. Pettersen, E. F. et al. UCSF Chimera-a visualization system for exploratory research and analysis. *J. Comput. Chem.* **25**, 1605–1612 (2004).
92. Bushnell, G. W., Louie, G. V. & Brayer, G. D. High-resolution three-dimensional structure of horse heart cytochrome c. *J. Mol. Biol.* **214**, 585–595 (1990).
93. Jo, S., Kim, T., Iyer, V. G. & Im, W. CHARMM-GUI: a web-based graphical user interface for CHARMM. *J. Comp. Chem.* **29**, 1859–1865 (2008).
94. Autenrieth, F., Tajkhorshid, E., Baudry, J. & Luthey-Schulten, Z. Classical force field parameters for the heme prosthetic group of cytochrome c. *J. Comput. Chem.* **25**, 1613–1622 (2004).
95. Phillips, J. et al. Scalable molecular dynamics with NAMD. *J. Comput. Chem.* **26**, 1781–1802 (2005).
96. Koes, D. R., Baumgartner, M. P. & Camacho, C. J. Lessons learned in empirical scoring with smina from the CSAR 2011 benchmarking exercise. *J. Chem. Inf. Mod.* **53**, 1893–1904 (2013).
97. Zoete, V., Cuendet, M. A., Grosdidier, A. & Michielin, O. SwissParam: a fast force field generation tool for small organic molecules. *J. Comp. Chem.* **32**, 2359–2368 (2011).
98. Bakan, A., Meireles, L. M. & Bahar, I. ProDy: protein dynamics inferred from theory and experiments. *Bioinformatics* **27**, 1575–1577 (2011).

Acknowledgements

The study was supported by the National Institutes of Health grant GM134715 (to V.E.K. and M.L.G.), HL117880 (M.L.G.), NS076511 (V.E.K. and H.B.) and AG059683 (R.W.), the Polish National Science Centre (2019/35/D/ST4/02203 to K.M.-R) and the Natural Sciences and Engineering Research Council of Canada (RGPIN/5368-2019 to G.M.H). G.M.H. is the Canada Research Chair in Molecular Cardiolipin Metabolism.

Author contributions

Conceptualization was the responsibility of V.E.K., H.B. and M.L.G. Methodology was the responsibility of V.E.K., Y.Y.T., V.A.T., A.A.K., A.A.A., J.P., J.J., R.W., M.L.G., P.C.A.W., A.L., G.M.H. and E.V.N. Software was the responsibility of Y.Y.T., K.M.-R. and P.C.A.W. Validation was carried out by V.E.K. and M.L.G. Formal analysis was conducted by Y.Y.T., V.A.T., A.A.K., A.A.A., S.N.S., M.A.A., G.K.V., E.-K.B., D.D., J.J. and A.R. Computational modeling was carried out by K.M.-R. and I.B. Investigation was conducted by Y.Y.T., V.A.T., A.A.K., M.A.A., S.N.S., H.H.D., A.B.S., A.K., Z.L., D.D., J.J., A.R., P.L., A.L., P.R., L.K.C., E.V.N. and K.K. Resources were the responsibility of K.M.-R., M.W.S., B.K., G.M.H., A.N., H.B., J.A. and J.V. Data curation was carried out by Y.Y.T., K.M.-R. and P.C.A.W. Writing of the original draft was carried out by V.E.K., H.B. and M.L.G. Review and editing was carried out by Y.Y.T., K.M.-R., P.C.A.W., M.W.S., I.B., G.M.H. and E.V.N. Visualization was the responsibility of Y.Y.T., K.M.-R., A.R. and A.L. Supervision was the responsibility of V.E.K., R.W., M.L.G., P.C.A.W. and J.V. Project administration was the responsibility of V.E.K. and M.L.G. Funding acquisition was the responsibility of V.E.K. and M.L.G.

Competing interests

The authors declare no competing interests.

Additional information

Extended data is available for this paper at https://doi.org/10.1038/s42255-023-00926-4.

Supplementary information The online version contains supplementary material available at https://doi.org/10.1038/s42255-023-00926-4.

Correspondence and requests for materials should be addressed to Valerian E. Kagan, Hülya Bayir or Miriam L. Greenberg.

Peer review information *Nature Metabolism* thanks Steven M. Claypool, Rafael Radi and the other, anonymous, reviewers for their contribution to the peer review of this work. Primary Handling Editor: Yanina-Yasmin Pesch, in collaboration with the *Nature Metabolism* team.

Reprints and permissions information is available at www.nature.com/reprints.

Publisher's note Springer Nature remains neutral with regard to jurisdictional claims in published maps and institutional affiliations.

[1]Department of Environmental and Occupational Health, Center for Free Radical and Antioxidant Health, School of Public Health, Children's Neuroscience Institute, University of Pittsburgh, Pittsburgh, Pennsylvania, USA. [2]Institute of Physics, Faculty of Physics, Astronomy and Informatics, Nicolaus Copernicus University in Toruń, Toruń, Poland. [3]Department of Physiology, Wayne State University School of Medicine, Detroit, MI, USA. [4]Department of Pediatrics, Genetic and Genomic Medicine Division, UPMC Children's Hospital of Pittsburgh, University of Pittsburgh, Pittsburgh, PA, USA. [5]Zernike Institute for Advanced Materials, University of Groningen, Groningen, The Netherlands. [6]Department of Biological Sciences, Wayne State University, Detroit, MI, USA. [7]Department of Biological Sciences, University of Pittsburgh, Pittsburgh, PA, USA. [8]Department of Pediatrics, Division of Critical Care and Hospital Medicine, Redox Health Center, Vagelos College of Physicians and Surgeons, Columbia University Irving Medical Center, New York, NY, USA. [9]Department of Pharmacology and Therapeutics, University of Manitoba, Children's Hospital Research Institute of Manitoba, Winnipeg, Manitoba, Canada. [10]Department of Pediatrics, Pediatric Institute for Heart Regeneration and Therapeutics, University of Pittsburgh, Pittsburgh, PA, USA. [11]Department of Chemistry & Centre for Biotechnology, Brock University, St Catharines, Ontario, Canada. [12]Laufer Center for Physical Quantitative Biology and Department of Biochemistry and Cell Biology, School of Medicine, Stony Brook University, New York, NY, USA. ✉e-mail: kagan@pitt.edu; hb2753@cumc.columbia.edu; mgreenberg@wayne.edu

https://doi.org/10.1038/s42255-023-00926-4

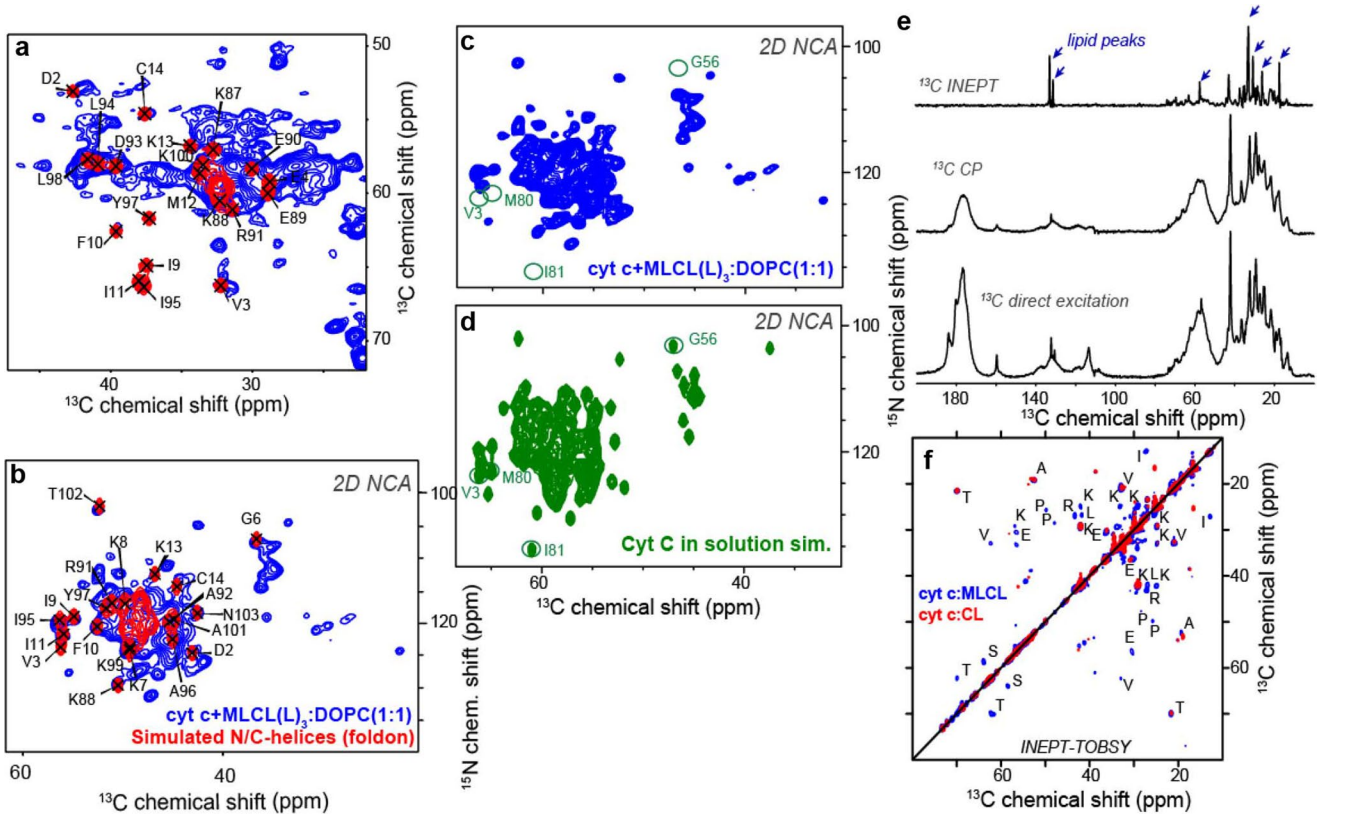

Extended Data Fig. 1 | SSNMR analysis of structural and dynamic rearrangements in the cyt c peroxidase complex with MLCL. a, Region from the 2D CP-DARR spectrum of ^{15}N,^{13}C-labeled cyt c bound to DOPC:MLCL$(L)_3$ (1:1; blue). Overlaid red contours show simulated peak patterns constructed from the solution NMR shifts of the N- and C-terminal α-helices (BMRB ID 25908). **b**, 2D ^{15}N-^{13}C NCA ssNMR spectrum of the same sample, along with a corresponding simulated spectrum for the N- and C-terminal α-helices. The simulated peaks from the blue foldon coincide with strong peaks in the experimental ssNMR spectra. **c**, 2D (CP-based) ^{15}N-^{13}C NCA ssNMR spectrum of membrane-bound cyt c, alongside the analogous simulated spectrum (**d**) for cyt c in solution (BMRB ID 25908). Key resonances missing in the experimental spectrum (**c**) are indicated with green circles; these mostly belong to the Ω-loop D (for example Met_{80} and Ile_{81}). These 2D NCA ssNMR spectra were acquired at 253 K and 10 kHz MAS. **e**, 1D ^{13}C INEPT, CP, and direct excitation spectra of ^{15}N,^{13}C-labeled cyt c bound to DOPC:MLCL$(L)_3$ (1:1), measured at 278K. These ssNMR spectra detect flexible (INEPT), rigid (CP), or both (direct excitation) sample components. The liquid crystalline lipids contribute many peaks to the INEPT spectrum (marked with blue arrows), while the labeled protein dominates the other two spectra. **f**, Overlay of 2D INEPT-TOBSY spectra for ^{15}N,^{13}C-labeled cyt c bound to MLCL/DOPC (blue) and CL/DOPC (red) vesicles. Cross-peaks stem from the labeled protein and must reflect flexible residues. Many more (and stronger) peaks are seen for MLCL-bound cyt c.

https://doi.org/10.1038/s42255-023-00926-4

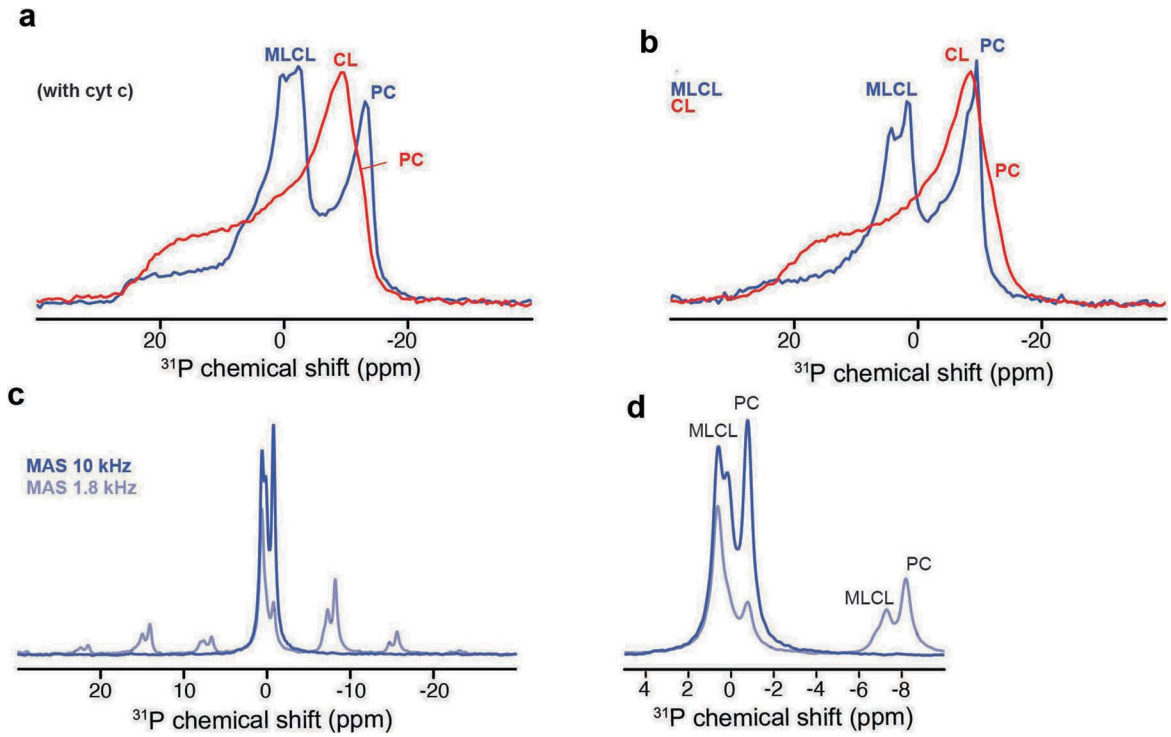

Extended Data Fig. 2 | ^{31}P ssNMR analysis of MLCL-induced structural and dynamic changes in the lipid membrane. a, 1D ^{31}P ssNMR static spectra of DOPC:MLCL (1:1) (blue) and DOPC:CL (1:1) (red) vesicles with bound cyt c. **b**, Analogous ^{31}P NMR spectra in absence of cyt c. Panels (**a**,**b**) show that the presence of MLCL results in a narrower extra component, that is neither isotropic nor reflects a typical non-bilayer phase. As previously discussed[23], these signals reflect MLCL in the liquid crystalline bilayer, undergoing distinct, increased dynamics (of the phosphate groups) compared to normal CL. **c**, 1D ^{31}P ssNMR MAS spectra of DOPC:MLCL (1:1) at 10 kHz (blue curve) and 1.8 kHz (light blue curve) MAS rates. **d**, Zoomed-in region from (C) showing the isotropic peak (left) and first sideband (at 1.8 kHz MAS). Peak assignments are indicated, based on prior publications[13,23]. Note that in the side bands, the PC signals are strong, one MLCL signal is partly retained and one MLCL signal is attenuated or missing. This is consistent with the shown assignments and cited literature.

https://doi.org/10.1038/s42255-023-00926-4

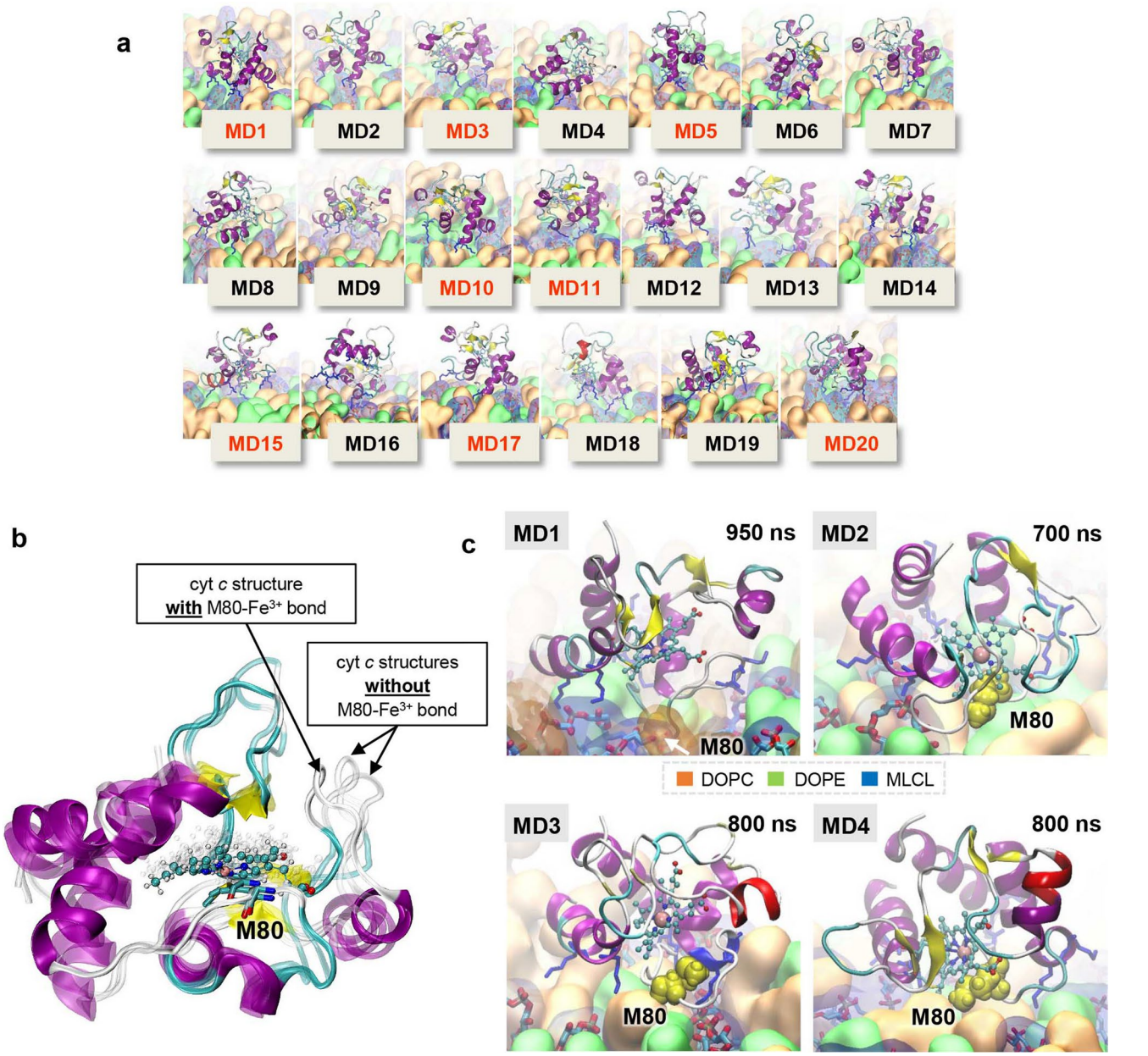

Extended Data Fig. 3 | Final shapshots from simulations of cyt c – membrane interactions and superposition of the conformations of cyt c reached after 100 ns runs. a, Final shapshots from simulations of cyt c – membrane interactions, and residues making frequent contacts with MLCL. Final conformations of cyt c reached after 100 ns in twenty independent MD trajectories. *Red labels* denote the systems which were further extended to 300 ns. The colors of the components of the membrane are following: DOPC – *in orange*, DOPE – *in green*, MLCL – *in transparent blue*. **b**, Superposition of the conformations of cyt c reached after 100 ns runs, in a system without membrane which contained Fe-S bond (*sharp structure*) and two independent runs where the bond was drastically weakened (*transparent structures*). All final conformations of heme group are displayed as *grey shadow balls-sticks*. **c**, Final conformations of cyt c after association with the membrane, observed in four runs MD1-MD4 (labeled). The *white arrow* in the upper left panel shows the residue M_{80} which inserted deep into the membrane, being trapped by several MLCL molecules, also shown in Fig. 2b.

https://doi.org/10.1038/s42255-023-00926-4

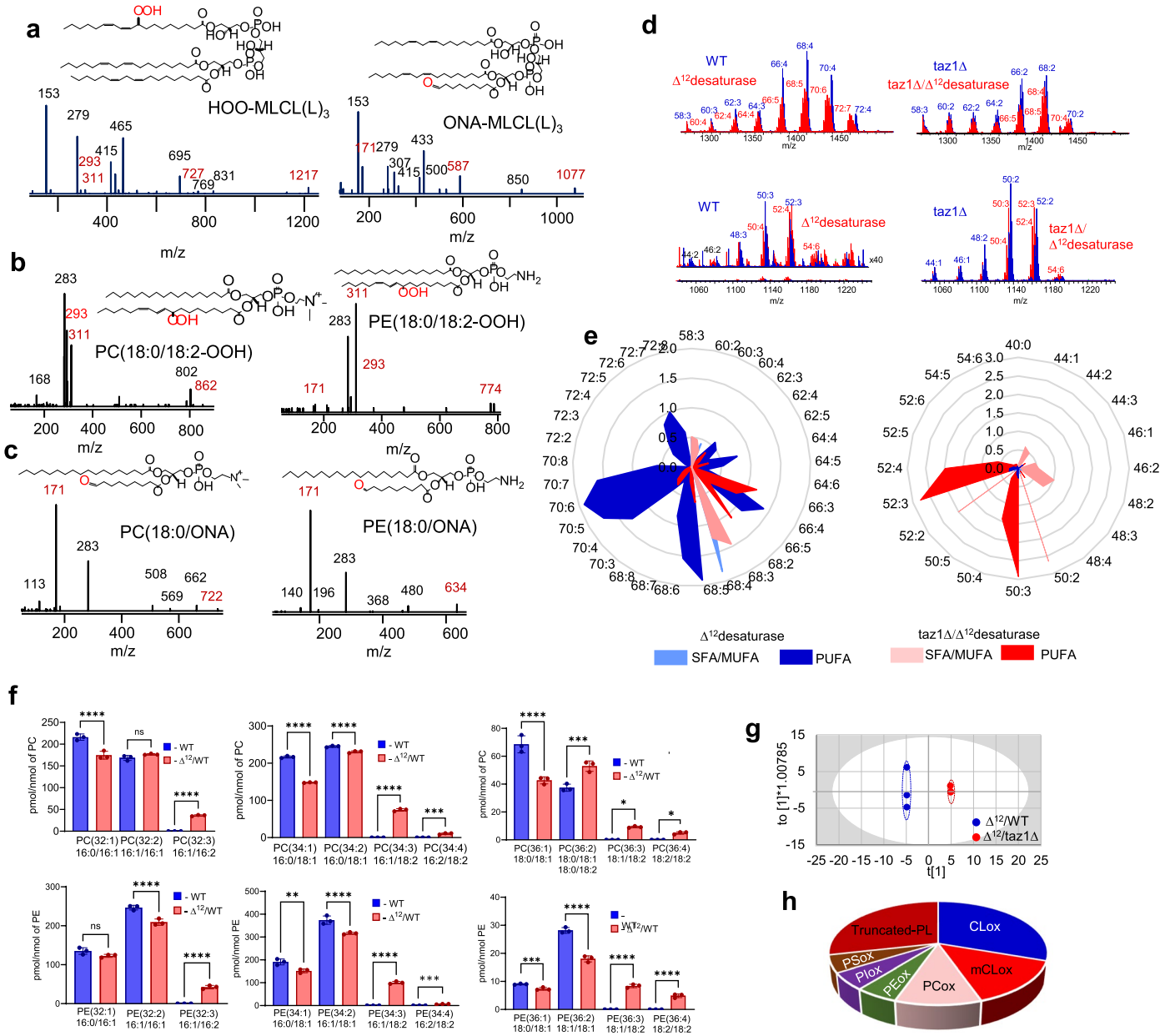

Extended Data Fig. 4 | Peroxidase activity of cyt c–MLCL complex causes phospholipid peroxidation in vitro and induces changes in lipidome and oxy-lipidome of genetically manipulated yeast. MS/MS spectra of (**a**) HOO-MLCL(L)$_3$ (left panel) and oxidatively truncated ONA-MLCL(L)$_3$ (right panel), (**b**) PC(18:0/18:2-OOH) (left panel) and PE(18:0/18:2-OOH) (right panel), (**c**) PC(18:0/ONA) (left panel) and PE(18:0/ONA) (right panel). Possible structures of oxidation products are inserted. ONA- 9-oxo nonanoic acid. **d**, Typical MS spectra of CL (upper panels) and MLCL (lower panels) obtained from yeast cells. **e**, Effect of D^{12}desaturase on composition of CL (left panel) and MLCL (right panel) in WT and taz1D yeasts. SFA – saturated fatty acids, MUFA – monounsaturated fatty acids, PUFA – polyunsaturated fatty acids. **f**, Content of PC (upper panels) and PE (lower panels) molecular species in WT and D^{12}/*taz1*D cells. Data are presented as mean values ± SD. Each data point represents a biologically independent sample. Upper panels: left ****P < 0.0001, middle ****P < 0.0001, ***P = 0.0004, right *P = 0.0202, ***P = 0.0001. ****P < 0.0001. One-way ANOVA, Tukey's multiple comparison test. Lower panels; left ****P < 0.0001, middle **P = 0.0115. ***P = 0.0006, unpaired two-tailed t-test, ***P < 0.0001, ****P < 0.0001, One-way ANOVA, Tukey's multiple comparison test. right ***P = 0.0056, unpaired two-tailed t-test, ****P < 0.0001, One-way ANOVA, Tukey's multiple comparison test. **g**, OPLS-DA analysis showing the differences in oxy-lipidomes of D^{12} and D^{12}/taz1D yeast cells; **h**, Pie plots showing the number of oxidatively modified phospholipid species. In total, 60 oxygenated phospholipid species were detected in yeast cells.

https://doi.org/10.1038/s42255-023-00926-4

a

		Clinical information	Age (yr)	Sex
#1	Control	Non-failing LV	23	Male
#2	Control	Non-failing LV	4	Female
#3	Control	Non-failing LV	4	Male
#4	NBHF	Tricuspid atresia LV	5	Female
#5	NBHF	Cardiomyopathy LV	11	Female
#6	NBHF	Dilated cardiomyopathy LV	13	Male
#7	BTHS	Transplant LV	4	Male
#8	BTHS	Transplant LV	13	Male
#8	BTHS	Transplant RV	13	Male

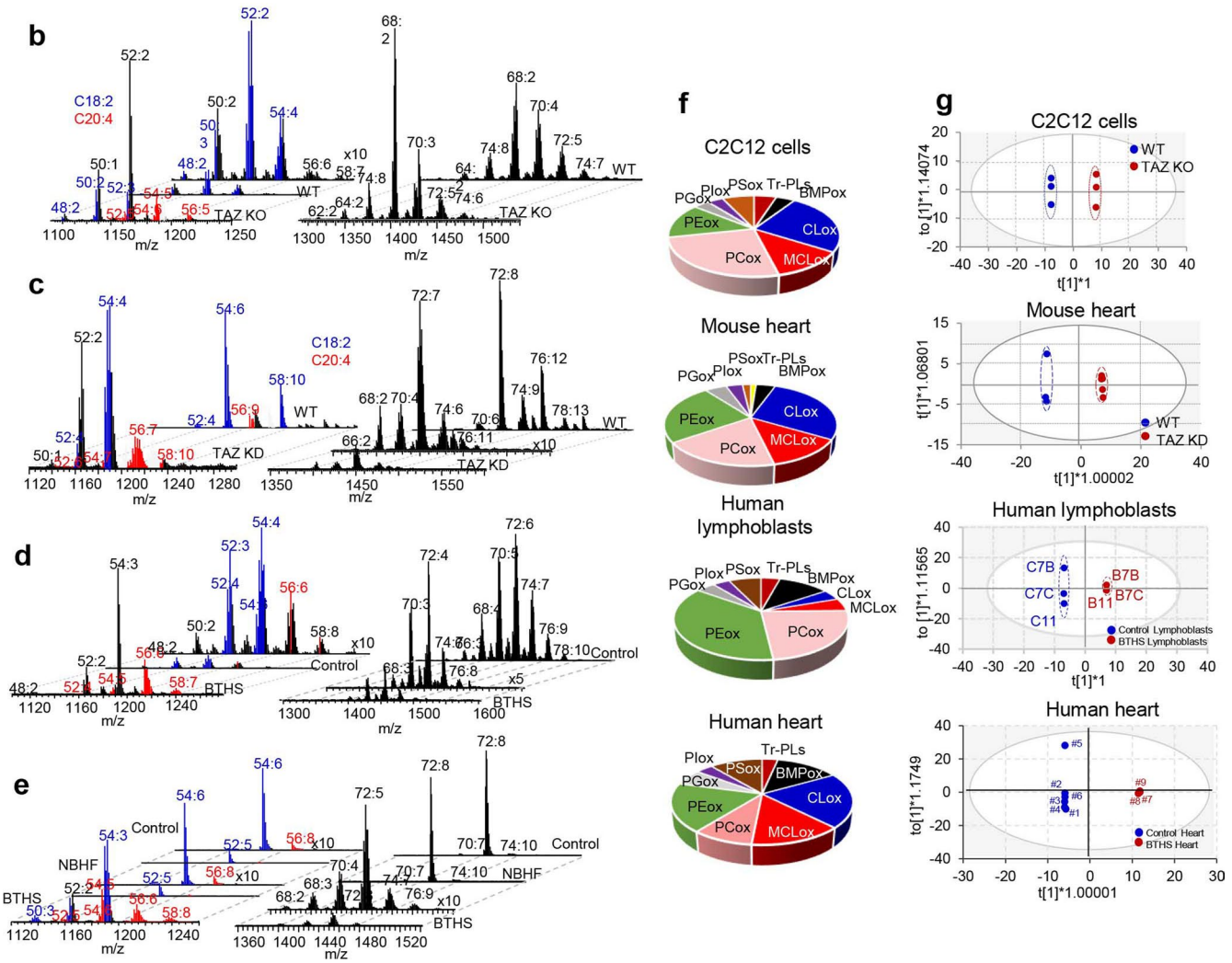

Extended Data Fig. 5 | TAZ deficiency induces the changes in phospholipidome of mouse myoblasts and human lymphoblasts *in vitro* and mouse and human heart *in vivo*. a, Table: Human heart biopsy sample description. Typical spectra of MLCL (left panels) and CL (right panels) obtained from WT and TAZ-KO C2C12 cells (**b**), WT and TAZ-KD mice (**c**), human lymphoblasts (**d**) and heart biopsy samples from control, non-BTHS-associated heart failure (NBHF) and BTHS-associated heart failure (BTHS) patients (**e**). TAZ deficiency in cells and mice and TAZ mutation in human results in a decrease of MLCL molecular species with C18:2 and appearance of MLCL molecular species containing C20:4 (shown in red); (**f**) Pie plots showing the total number of MLCL species in C2C12 cells, mouse heart, human lymphoblasts and heart samples from BTHD patients. (**g**) The score plots of OPLS-DA analysis show the differences in oxy-lipidomes in WT and TAZ-KO cells, WT and TAZ-KD mice, human control and BTHS lymphoblasts and control heart samples and BTHS heart samples.

https://doi.org/10.1038/s42255-023-00926-4

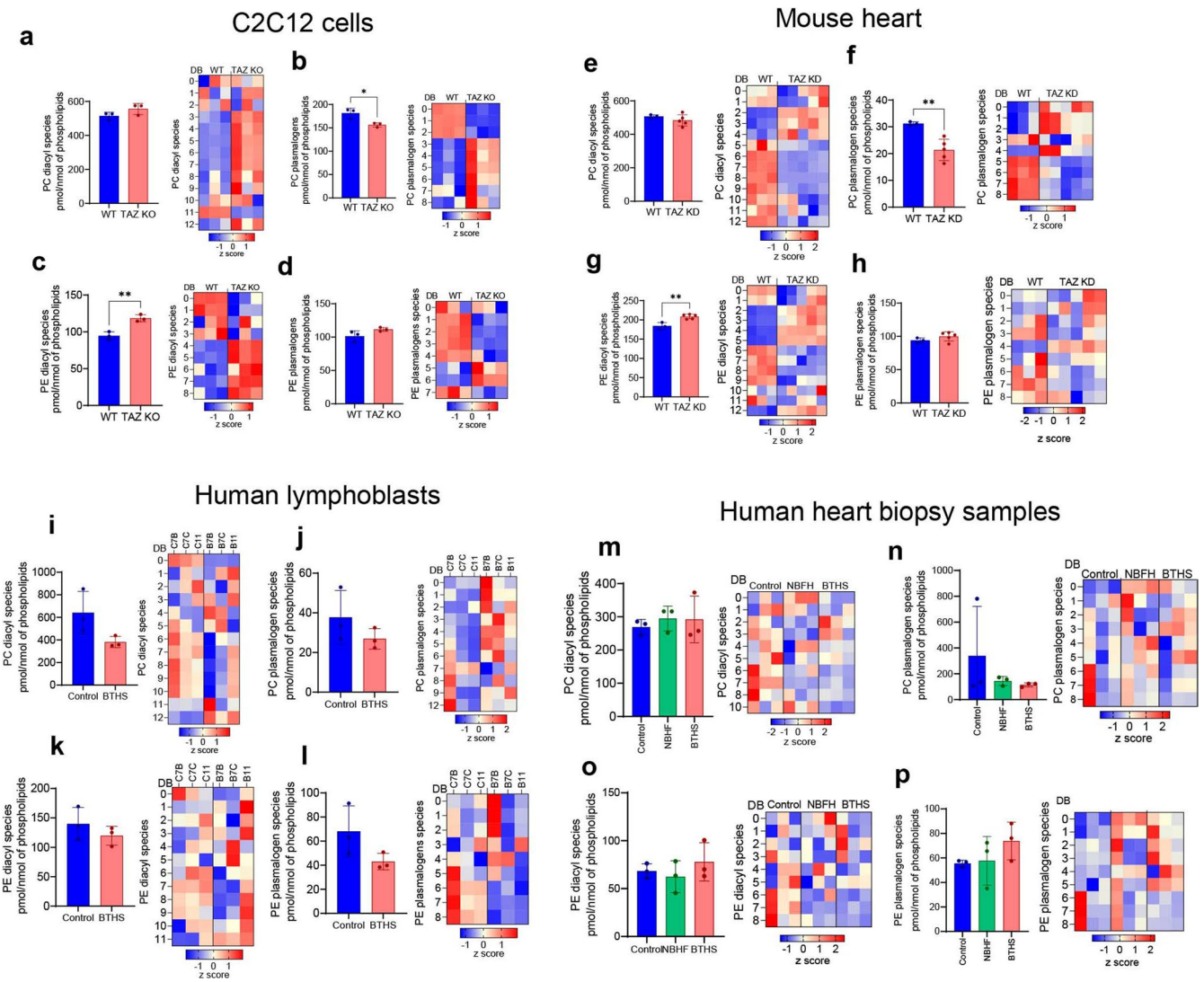

Extended Data Fig. 6 | Content of PE and PC species in cells, mouse heart, human lymphoblasts and human heart biopsy samples. C2C12 cells (a-d): **a**, Total content of diacyl-PC (left panel) and its molecular species (right panel). **b**, Total content of plasmalogen-PC (left panel) and its molecular species (right panel). **c**, Total content of diacyl-PE (left panel) and its molecular species (right panel). **d**, Total content of plasmalogen-PE (left panel) and its molecular species (right panel). **Mouse heart (e-h): e**, Total content of diacyl-PC (left panel) and its molecular species (right panel). **f**, Total content of plasmalogen-PC (left panel) and its molecular species (right panel). **g**, Total content of diacyl-PE (left panel) and its molecular species (right panel). **h**, Total content of plasmalogen-PE (left panel) and its molecular species (right panel). **Human lymphocytes (i-l): i**, Total content of diacyl-PC (left panel) and its molecular species (right panel). **j**, Total content of plasmalogen-PC (left panel) and its molecular species (right panel). **k**, Total content of diacyl-PE (left panel) and its molecular species (right panel). **l**, Total content of plasmalogen-PE (left panel) and its molecular species (right panel). Human heart biopsy samples (m-p): **m**, Total content of diacyl-PC (left panel) and its molecular species (right panel). **n**, Total content of plasmalogen-PC (left panel) and its molecular species (right panel). **o**, Total content of diacyl-PE (left panel) and its molecular species (right panel). **p**, Total content of plasmalogen-PE (left panel) and its molecular species (right panel). *P < 0.05, **P < 0.01. DB - double bond number.

https://doi.org/10.1038/s42255-023-00926-4

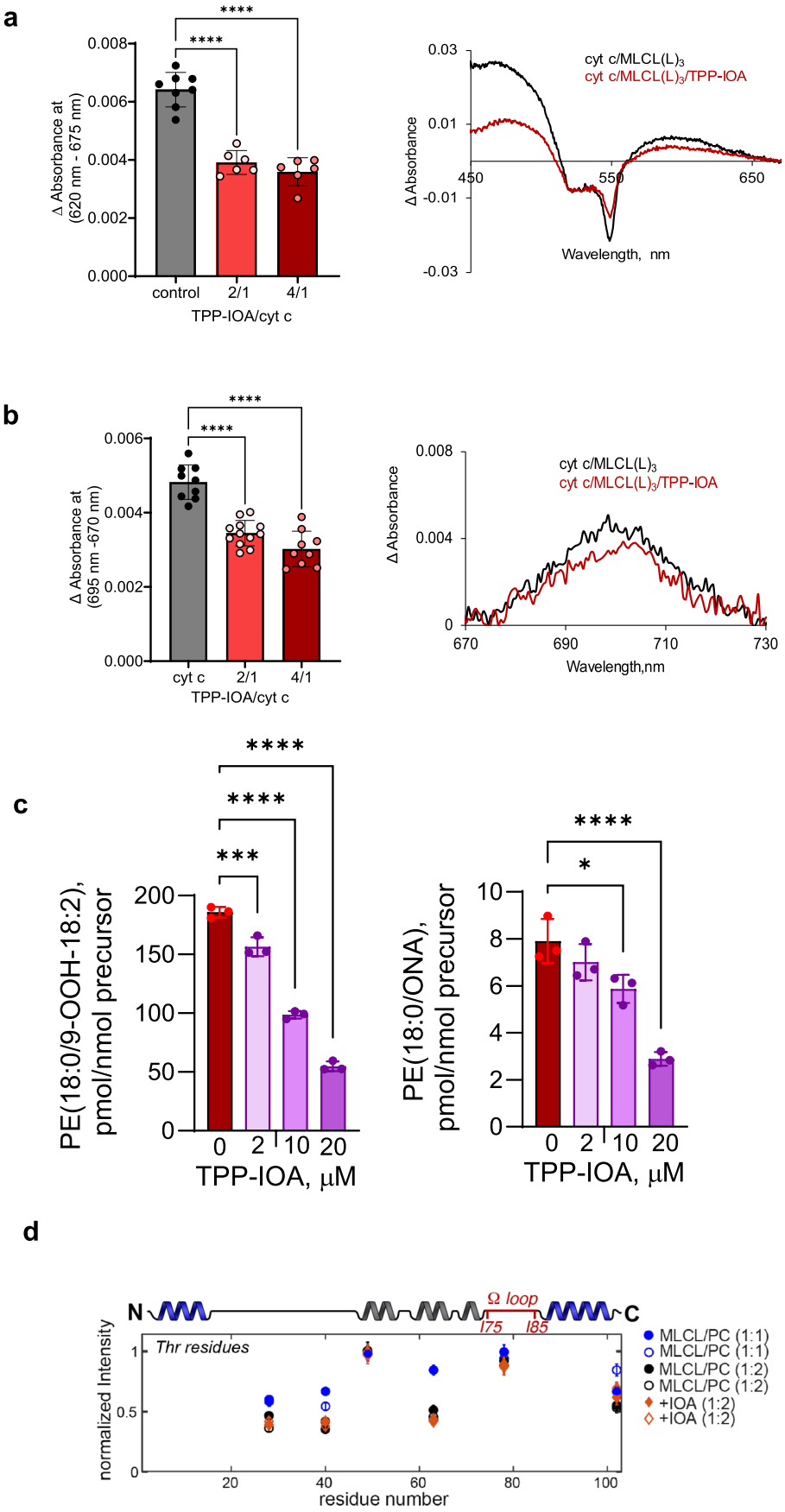

Extended Data Fig. 7 | See next page for caption.

https://doi.org/10.1038/s42255-023-00926-4

Extended Data Fig. 7 | Effect of TPP-IOA on structure of cyt c–MLCL peroxidase complex, with MLCL, lipid oxidation and the endurance of *Drosophila melanogaster*. Effect of TPP-imidazole-oleic acid (TPP-IOA) on MLCL$(L)_3$-dependent formation of heme iron high-spin forms assessed by absorbance at 620 nm (**a**) and absorbace at 695 nm (**b**). Right: the differential absorption spectra (**a**) and representative absorption spectra (**b**) of MLCL–cyt c with or without TPP-IOA. Data are presented as mean values ± SD. Each data point represents a biologically independent sample. ****p < 0.0001, One-way ANOVA, Tukey's multiple comparison test. (**a**) N = 8 (control), N = 6 (TPP-IOA–cyt c = 2/1), N = 6 (TPP-IOA–cyt c = 4/1). (**b**) N = 8 (control), N = 10 (TPP-IOA–cyt c = 2/1), N = 9 (TPP-IOA–cyt c = 4/1).(**c**) TPP-IOA inhibits accumulation of HOO-PE (left panel) and oxidatively truncated PE (right panel) species formed in MLCL$(L)_3$–cyt c-driven reaction. Data are presented as mean values ± SD. N = 3. Each data point represents a biologically independent sample. Right panel: *p = 0.0287, ****p < 0.0001, Left panel: ***p = 0.0007, ****p < 0.0001. One-way ANOVA, Tukey's multiple comparison test. (**d**) Normalized peak intensity values from ^{13}C-^{13}C ssNMR spectra of cyt c bound to DOPC:MLCL$(L)_3$ (1:1; blue), or DOPC:MLCL$(L)_3$ (2:1) LUVs in the absence (black) and presence (orange) of a four-fold excess of IOA with respect to protein (1:40 P/L ratio). Shown are the Cα/Cβ (open) and Cβ/Cα (closed) peaks for Thr residues. Each residue shows two data points: one for either side of the diagonal: see Fig. 5e). Increasing the ratio of MLCL (over PC) caused a net decrease in peak intensities, signifying increased protein motion. Addition of the IOA inhibitor had a much more modest effect on the Thr peak volumes.

https://doi.org/10.1038/s42255-023-00926-4

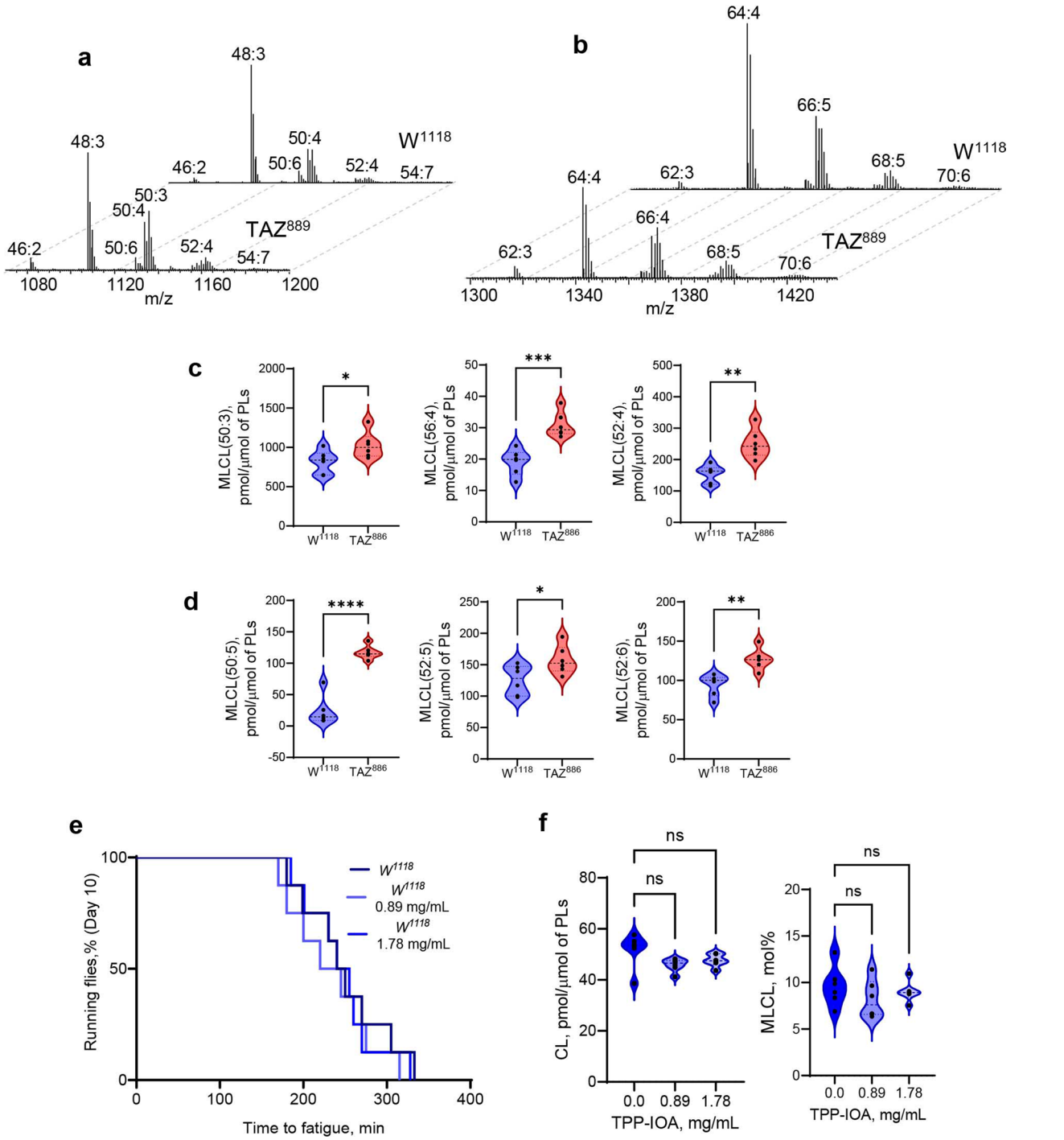

Extended Data Fig. 8 | TAZ deficiency induces changes in *Drosophila melanogaster* lipidome. Typical mass spectra of MLCL (**a**) and CL (**b**) obtained from control (W^{1118}) and (TAZ^{889}) mutant flies. Content MLCL containing C18:2 (**c**) and C18:3 (**d**) in control W^{1118} and TAZ^{889} deficient flies. Lipidomics analysis was performed using 6 vials (n = 20 fly torsos per vial). (**c**) *P = 0.0401, **P < 0.0015, ***P = 0.0005 unpaired two-tailed t-test. (**d**) *P = 0.0378, **P < 0.0019, ****p < 0.0001 unpaired two-tailed t-test. (**e**) TPP-IOA did not significantly affect the endurance of control flies. Endurance was measure using 8 vials (N = 20 flies) and significance was determined by log-rank analysis., ns = not significant. (**f**) Content of CL (left panel) and MLCL (right panel) in control W^{1118} flies after feeding with TPP-IOA. Lipidomics analysis was performed using 6 vials (n = 20 fly torsos per vial). For all violin plots presented, individual points including maximal and minimal are shown as black circles. Dashed black line indicates median and doted lines indicate quartiles.

nature portfolio

Corresponding author(s): Valerian E Kagan

Last updated by author(s): Aug 29, 2023

Reporting Summary

Nature Portfolio wishes to improve the reproducibility of the work that we publish. This form provides structure for consistency and transparency in reporting. For further information on Nature Portfolio policies, see our Editorial Policies and the Editorial Policy Checklist.

Statistics

For all statistical analyses, confirm that the following items are present in the figure legend, table legend, main text, or Methods section.

n/a	Confirmed	
☐	☒	The exact sample size (*n*) for each experimental group/condition, given as a discrete number and unit of measurement
☐	☒	A statement on whether measurements were taken from distinct samples or whether the same sample was measured repeatedly
☐	☒	The statistical test(s) used AND whether they are one- or two-sided *Only common tests should be described solely by name; describe more complex techniques in the Methods section.*
☒	☐	A description of all covariates tested
☐	☒	A description of any assumptions or corrections, such as tests of normality and adjustment for multiple comparisons
☐	☒	A full description of the statistical parameters including central tendency (e.g. means) or other basic estimates (e.g. regression coefficient) AND variation (e.g. standard deviation) or associated estimates of uncertainty (e.g. confidence intervals)
☐	☒	For null hypothesis testing, the test statistic (e.g. *F*, *t*, *r*) with confidence intervals, effect sizes, degrees of freedom and *P* value noted *Give P values as exact values whenever suitable.*
☒	☐	For Bayesian analysis, information on the choice of priors and Markov chain Monte Carlo settings
☒	☐	For hierarchical and complex designs, identification of the appropriate level for tests and full reporting of outcomes
☒	☐	Estimates of effect sizes (e.g. Cohen's *d*, Pearson's *r*), indicating how they were calculated

Our web collection on statistics for biologists contains articles on many of the points above.

Software and code

Policy information about availability of computer code

Data collection	VMD: A popular molecular graphics program, used to analyze and visualize simulation trajectories generated. This software is available for academic research purposes at: www.ks.uiuc.edu/Research/vmd/ PRoDy 2.0: Is a free and open-source Python software package or analysis of the simulation trajectories. This software is available at: prody.csb.pitt.edu. ssNMR data were acquired using AVANCE NEO 600 MHz (14.1 T) spectrometer from Bruker Biospin (Billerica, MA, USA). The molecular structure of cyt c was visualized using the UCSF Chimera program. Mass spectrometry data were acquired on Fusion Lumos mass spectrometer using Xcalibur 4.0 software. Median fluorescence intensity of single cells was analyzed by FlowJo software v10. MD simulations of cyt c were performed using the NAMD software.
Data analysis	Graphs were plotted using GraphPad Prism 9.0, Origin 2022b or Microsoft Excel. Mass spectrometry data were analyzed using Compound Discoverer 2.0, Xcalibur 4.0 and Microsoft Excel 2019. Orthogonal Projections to Latent Structures Discriminant Analysis was performed by using SIMCA 16 software. The ssNMR spectra were processed and peaks were integrated with the NMRPipe software package

For manuscripts utilizing custom algorithms or software that are central to the research but not yet described in published literature, software must be made available to editors and reviewers. We strongly encourage code deposition in a community repository (e.g. GitHub). See the Nature Portfolio guidelines for submitting code & software for further information.

Data

Policy information about availability of data

All manuscripts must include a data availability statement. This statement should provide the following information, where applicable:

- Accession codes, unique identifiers, or web links for publicly available datasets
- A description of any restrictions on data availability
- For clinical datasets or third party data, please ensure that the statement adheres to our policy

The authors declare that data generated or analyzed during the study and included in this published article are available from the corresponding author on request.

Human research participants

Policy information about studies involving human research participants and Sex and Gender in Research.

Reporting on sex and gender	Available clinical and demographic characteristics of the non-failing controls and patients are presented in the Extended data figure 4A.
Population characteristics	Available demographic characteristics of the non-failing controls and patients are presented in the Extended data figure 4A.
Recruitment	Discarded human myocardial samples were collected from patients undergoing heart surgery or heart transplantation
Ethics oversight	Discarded human myocardial samples were collected from patients undergoing heart surgery or heart transplantation [University of Pittsburgh Institutional Review Board (IRB) protocol STUDY19070300].

Note that full information on the approval of the study protocol must also be provided in the manuscript.

Field-specific reporting

Please select the one below that is the best fit for your research. If you are not sure, read the appropriate sections before making your selection.

☒ Life sciences ☐ Behavioural & social sciences ☐ Ecological, evolutionary & environmental sciences

For a reference copy of the document with all sections, see nature.com/documents/nr-reporting-summary-flat.pdf

Life sciences study design

All studies must disclose on these points even when the disclosure is negative.

Sample size	The chosen sample size produce suitable standard deviation.
Data exclusions	No data were excluded from analysis.
Replication	All attempts at replication of experimental findings were successful.
Randomization	All samples and animals were randomly allocated into experimental groups.
Blinding	Investigators were blinded to group allocation during data collection.

Reporting for specific materials, systems and methods

We require information from authors about some types of materials, experimental systems and methods used in many studies. Here, indicate whether each material, system or method listed is relevant to your study. If you are not sure if a list item applies to your research, read the appropriate section before selecting a response.

Materials & experimental systems

n/a	Involved in the study
☒	☐ Antibodies
☐	☒ Eukaryotic cell lines
☒	☐ Palaeontology and archaeology
☐	☒ Animals and other organisms
☒	☐ Clinical data
☒	☐ Dual use research of concern

Methods

n/a	Involved in the study
☒	☐ ChIP-seq
☐	☒ Flow cytometry
☒	☐ MRI-based neuroimaging

Eukaryotic cell lines

Policy information about cell lines and Sex and Gender in Research

Cell line source(s)	A commercially available mouse C2C12 myoblast cell line (ATCC, cat. #: CRL-1772). The TAZ-KO cell line was generated by CRISPR-mediated inactivation of TAZ in C2C12 myoblast cell line. Three BTHS lymphoblast cell lines (GM22164, GM22150, and GM22129) derived from clinically affected patients and characterized by loss-of-function mutations in TAZ, along with three lymphoblast lines derived from apparently healthy demographic-matched control individuals (AG14840, AG14798, AG14725) were obtained from the Coriell Institute for Medical Research (Camden, NJ).
Authentication	None of the cell lines used were authenticated.
Mycoplasma contamination	All cell lines were tested negatively for Mycoplasma contamination.
Commonly misidentified lines (See ICLAC register)	No commonly misidentified lines were used in this study.

Animals and other research organisms

Policy information about studies involving animals; ARRIVE guidelines recommended for reporting animal research, and Sex and Gender in Research

Laboratory animals	C57BL/6J mice (Jackson Laboratory, Bar Harbour, ME) and Drosophila melanogaster were used in the study
Wild animals	Study didn't involve wild animals.
Reporting on sex	Wild type male mice and male mice positive for the TAZ shRNA transgene were used in the study
Field-collected samples	Study didn't involve samples collected from field.
Ethics oversight	The mouse experiments were performed with approval of the University of Manitoba Animal Policy and Welfare Committee which adheres to the principles for biomedical research involving animals developed by the Canadian Council on Animal Care and the Council for International Organizations of Medical Sciences and was reported in accordance with ARRIVE guidelines.

Note that full information on the approval of the study protocol must also be provided in the manuscript.

Flow Cytometry

Plots

Confirm that:

☒ The axis labels state the marker and fluorochrome used (e.g. CD4-FITC).

☒ The axis scales are clearly visible. Include numbers along axes only for bottom left plot of group (a 'group' is an analysis of identical markers).

☒ All plots are contour plots with outliers or pseudocolor plots.

☒ A numerical value for number of cells or percentage (with statistics) is provided.

Methodology

Sample preparation	Cells were grown to the mid log phase, treated with 1 mM tBHP and stained with 2 mM BODIPY 581/591 C11 for 30 minutes.
Instrument	BD LSR II flow cytometer (BD Bioscience) was used
Software	Flow cytometry data were collected using BD FACSDiva software and analyzed with FlowJo v10.

Cell population abundance	The flow cytometer we used (BD LSR II) is not capable of cell sorting. Therefore, the post-sorting purity of the samples was not determined.
Gating strategy	On SSC vs. FSC, cells were gated to eliminate debris. On FSC-H vs. FSC-A, single cells were gated to eliminate cell aggregates. The cutoffs between positive and negative –BODIPY green– were set based on a combination of the unstained, single-stained controls (used as negative controls) and fully stained samples.

☐ Tick this box to confirm that a figure exemplifying the gating strategy is provided in the Supplementary Information.